2012

Scanning angle total internal reflection Raman spectroscopy and plasmon enhancement techniques as a tool for interfacial analysis

Kristopher James McKee
Iowa State University

Scanning angle total internal reflection Raman spectroscopy and plasmon enhancement techniques as a tool for interfacial analysis

by

Kristopher J. McKee

A dissertation submitted to the graduate faculty

In partial fulfillment of the requirements for the degree of

DOCTOR OF PHILOSOPHY

Major: Analytical Chemistry

Program of Study Committee

Emily A. Smith, Major Professor
Robert S. Houk
Patricia A. Thiel
Ning Fang
Joseph Burnett

Iowa State University

Ames, Iowa

2012

TABLE OF CONTENTS

ACKNOWLEDGEMENT iv

CHAPTER 1: GENERAL INTRODUCTION 1

Dissertation overview 1

Raman spectroscopy 2

Total internal reflection (TIR) Raman spectroscopy 4

TIR Raman spectroscopy at smooth metal films, (SPR) Raman spectroscopy 7

TIR Raman spectroscopy at plasmon waveguides, (PWR) Raman spectroscopy 10

References 13

Figures 15

CHAPTER 2: DEVELOPMENT OF A SCANNING ANGLE TOTAL INTERNAL REFLECTION RAMAN SPECTROMETER 21

Abstract 21

Introduction 22

Experimental 25

Results and discussion 28

Conclusions 34

Acknowledgement 34

References 35

Figures 37

CHAPTER 3: NEAR IR SCANNING ANGLE TOTAL INTERNAL REFLECTION RAMAN SPECTROSCOPY AT SMOOTH GOLD FILMS 45

Abstract 45

Introduction 46

Materials and methods 49

Results and discussion 52

Conclusions 58

Acknowledgement 59

References 60

Figures 63

Supporting information 70

CHAPTER 4: PLASMON WAVEGUIDE RESONANCE RAMAN SPECTROSCOPY 75

Abstract 75

Introduction 76

Materials and methods 78

Results and discussion 81

Conclusions 86

Acknowledgement 87

References 88

Figures 90

CHAPTER 5: GENERAL CONCLUSION 97

ACKNOWLEDGEMENT

This dissertation would not have been possible without the guidance of my research advisor, Dr. Emily Smith and my committee members Drs. Houk, Thiel, Burnett, and Fang. I would also like to thank the Iowa State University Department of Chemistry and the Ames Laboratory for providing the opportunity to perform this research. Additionally, I would like to thank all those close to me for their support during this endeavor.

This work was performed at the Ames Laboratory under contract number DE-AC02-07CH11358 with the U.S. Department of Energy. The document number assigned to this dissertation is IS-T 3052.

CHAPTER 1: GENERAL INTRODUCTION

Dissertation Overview

The focus of this dissertation is the development of a scanning angle total internal reflection (TIR) Raman microscope and TIR Raman signal enhancement techniques with a near infrared excitation source. Chapter 1 provides the motivation and background information including the fundamentals of TIR Raman spectroscopy, TIR Raman scattering from smooth noble metal films and TIR Raman scattering from plasmon waveguides.

Chapters 2 and 3 represent published manuscripts and Chapter 4 is a submitted manuscript on Raman scattering from plasmon waveguides. Chapter 2 provides a description of a prism based, scanning angle, TIR Raman microscope along with calibration and proof of concept experiments. Control of the incident angle of the excitation source in the TIR geometry provides a means to control the penetration depth of the electric field into the sample and thus the depth over which Raman scatter is collected in a sample. The collected Raman scatter at varying incident angles is correlated to the depth over which the signal is generated in the sample for a neat benzonitrile solution and a polystyrene film. A roughly 30-fold improvement in depth resolution is demonstrated in comparison to confocal Raman microscopy. The combination of low excitation powers at near-IR wavelengths, high background from the prism, and small sample volumes, however, led to relatively long acquisition times and therefore reproducible signal enhancement strategies were developed to reduce analysis time.

In Chapter 3, improvement of the scanning angle TIR Raman microscope and a Raman signal enhancement technique are described for the TIR geometry using a thin, smooth, gold film at the prism / sample interface as a means to increase the magnitude of the mean squared electric field (MSEF) encountered by the analyte and thus increase the generated Raman scatter. The inclusion of a gold film provided benefits including reduction of the background from the TIR prism, a decrease in the percent relative uncertainty in Raman peak areas, and an increase in the Raman signal relative to the amount of analyte probed. Monolayer sensitivity for non-resonant analytes is also demonstrated for the first time using TIR Raman spectroscopy with 785 nm excitation.

Chapter 4 describes the use of plasmon waveguide resonance (PWR) sensors in TIR Raman spectroscopy. PWR sensors consist of a thin gold film and a dielectric coating which acts as an electric field amplifier. Raman scatter is generated with p- and s-polarized incident light inducing electric fields polarized both parallel and perpendicular to the sample plane which is not possible at a smooth metal film. Enhanced Raman scatter was measured for aqueous pyridine and a thin polystyrene film at gold / SiO_2 plasmon waveguide. This technique adds a chemically specific detection method for events at an interface if compared to conventional PWR spectroscopy, and the ability to control the polarization of the excitation field if compared to SPR Raman spectroscopy.

Raman spectroscopy

In 1928, Krishna and Raman experimentally demonstrated the inelastic scattering of light from molecules and the technique later came to be known as Raman Spectroscopy.[1] Raman scattering occurs when monochromatic light with frequency v_0 encounters a molecule

and is scattered with frequencies higher, $v_{AS}=v_0+v_j$ (Anti-Stokes), and lower, $v_S=v_0-v_j$ (Stokes) than the excitation source (Figure 1). Most of the incident light is scattered with no change in frequency (i.e. $v_R=v_0$) and is known as Rayleigh scattering. Anti-Stokes Raman scattering is less intense than Stokes Raman scattering since the molecules must be in the first excited vibrational level, which has a lower population than the ground state at room temperature.[2] The probability of Raman scattering in general is low with approximately 1 in 10^{10} incident photons undergoing the process. Stokes Raman scattering was utilized in all experiments mentioned in the following chapters and will be considered exclusively for the remainder of this thesis. The change in frequency of the scattered light, (v_0-v_j), corresponds to excited vibrational modes in the molecule. For a vibrational mode to be Raman active there must be a change in the polarizability of the molecule, which is in contrast to the complimentary vibrational spectroscopy technique of IR-absorption spectroscopy where there must be a change in dipole moment. A change in polarizability can be described as a perturbation of the electron cloud with respect to the vibrational mode. There are *3N-5, or 3N-6* vibrational modes for linear and non-linear molecules with *N* atoms, respectively. The general equation for the intensity of Stokes Raman (P_R) scatter in units of photons/second is:

$$P_R = P_0 \sigma_j^{\circ} \nu_0 (\nu_0 - \nu_j)^3 D \, dz \tag{0.1}$$

where P_0 is the incident photon flux, σ_j° is the frequency independent cross section for the *j*th molecular vibration mode, *D* is the number density of scatterers, *dz* is the path length of the laser in the sample and all frequency terms, (v), are expressed in wavenumbers (cm^{-1}). A full derivation of this equation can be found elsewhere.[3] The selection of a laser source is an important experimental consideration due to the $v_0(v_0-v_j)^3$ dependence of the Raman signal.

While visible excitation will produce more Raman scatter than near-IR or mid-IR excitation, competing phenomena such as fluorescence observed at lower wavelengths can often obfuscate the Raman signal. In the present work near-IR excitation at 785 nm is used in an effort to minimize the fluorescent background. Key benefits of Raman spectroscopy are its non-destructive nature and aqueous sampling capabilities.

TIR Raman spectroscopy

Raman Spectroscopy is not an inherently surface sensitive technique; however, the TIR sampling geometry provides a means to control the probe depth in a sample within a few microns of the surface (Figure 2a). TIR occurs at an interface between two materials with refractive indices η_1 and η_2, where $\eta_1 > \eta_2$ with light travelling from the more optically dense medium to the optically rarer medium at an angle greater than or equal to the critical angle (θ_C) as defined in Eq. 1.2.

$$\theta_C = \sin^{-1} \eta_2 / \eta_1 \tag{0.2}$$

Under TIR, the light does not penetrate the optically rarer medium; however, an evanescent wave is generated that penetrates the lower refractive index material due to boundary conditions at the interface.[4] The depth at which the evanescent wave decreases to 1/e is the penetration depth, d_p:

$$d_p = \frac{\lambda}{2\pi}\left(\eta_1^2 \sin^2 \theta - \eta_2^2\right)^{-\frac{1}{2}} \tag{0.3}$$

where λ is the wavelength and θ is the incident angle of the excitation source. The depth over which Raman scatter is generated, D_{RS}, is $d_p/2$ since Raman scatter is proportional to E^2, thus decreasing twice as fast as the evanescent wave.[5] For a given interface, D_{RS} is at a maximum at the critical angle and decreases with increasing incident angle. D_{RS} typically ranges from a few microns to tens of nanometers depending on the interface and wavelength of excitation (Figure 3). The D_{RS} equation indicates a practical way to obtain information from various depths in a sample is to control the incident angle of the excitation beam.

Fresnel factors (T_x, T_y, *and* T_z) describe the amplification factor of the electric field at the prism sample interface where *xy* is the sample plane and *z* extends perpendicularly from the interface. Parallel (p-) polarized incident light results in electric field oscillations in the *x* and *z* directions and perpendicularly (s-) polarized incident light produces oscillations in the *y* plane.[6] The Fresnel factors can be calculated as:

$$T_x = \frac{2\cos\theta_i(\sin^2\theta_i - \eta^2) + 2i\eta^2\cos^2\theta_i\sqrt{\sin^2\theta_i - \eta^2}}{\eta^4\cos^2\theta_i + \sin^2\theta_i - \eta^2} \tag{0.4}$$

$$T_y = \frac{2\cos^2\theta_i - 2i\cos\theta_i\sqrt{\sin^2\theta_i - \eta^2}}{1 - \eta^2} \tag{0.5}$$

$$T_z = \frac{2\eta^2\cos^2\theta_i\sin\theta_i - 2i\cos\theta_i\sin\theta_i\sqrt{\sin^2\theta_i - \eta^2}}{\eta^4\cos^2\theta_i + \sin^2\theta_i - \eta^2} \tag{0.6}$$

where θ_i is the incident angle and $\eta = \eta_2/\eta_1$. The respective electric fields can be calculated as $|T_{x,y,z}|^2 E_0$ (Figure 4b). The implication of the Fresnel factors is that the electric field is increased at the prism / sample interface under total internal reflection compared to normal illumination. For example, the electric field at the critical angle is calculated to be between

~5x (η_{sample} = 1.57) or ~7x (η_{sample} = 1.33) the incident electric field with 785 nm excitation at a sapphire/sample interface. Additionally, excitation with different polarizations can provide molecular orientation information as well as anisotropic refractive index determinations since the resultant evanescent waves have perpendicular polarizations.[7]

The reflected light from the interface can also be collected and provides valuable information in a TIR Raman experiment. The critical angle for a given interface is marked by a sharp increase in the reflected light intensity (Figure 4a). The reflection coefficients for s- and p-polarized incident light, R_s and R_p, respectively, can be calculated as:

$$R_s = \left| \frac{\eta_1 \cos\theta_i - \eta_2 \sqrt{1 - \left(\frac{\eta_1}{\eta_2} \sin\theta_i \right)^2}}{\eta_1 \cos\theta_i + \eta_2 \sqrt{1 - \left(\frac{\eta_1}{\eta_2} \sin\theta_i \right)^2}} \right|^2 \tag{0.7}$$

$$R_p = \left| \frac{\eta_1 \sqrt{1 - \left(\frac{\eta_1}{\eta_2} \sin\theta_i \right)^2} - \eta_2 \cos\theta_i}{\eta_1 \sqrt{1 - \left(\frac{\eta_1}{\eta_2} \sin\theta_i \right)^2} + \eta_2 \cos\theta_i} \right|^2 \tag{0.8}$$

Using the reflected light intensity from the interface, determination of the critical angle for a given interface and the refractive indices of interfacial species can be determined at the incident wavelength, all of which are key parameters for modeling the Raman scatter generated at an interface.

The first TIR Raman spectra were reported in 1973[8] and the surface sensitivity of the technique was later shown using polymer stacks where Raman scatter from a thin (≈ 1μm) polystyrene film at the prism interface was collected without contribution from a bulk polyethylene below.[9-10] Since then, TIR Raman spectra have been collected from a variety of solid-solid, solid-liquid, and liquid-liquid interfaces with the majority of work utilizing visible excitation sources or fixed excitation angles.[10-22] The versatility of TIR-Raman spectroscopy is illustrated by the wide variety of samples that have been analyzed including polymer films, epicuticular wax layers on leaves, adsorbates from solution, and lubricants at frictional contacts.[5] A key advance in TIR Raman spectroscopy was the inclusion of high efficiency microscope optics as a means to collect the Raman scatter from the analyte.[4] In Chapter 2, a high angular resolution (0.05˚) scanning angle TIR Raman microscope is described for control of D_{RS} utilizing 785 nm excitation to minimize background fluorescence.[23] Since Raman spectroscopy is an inherently low signal technique, excitation volumes in the TIR geometry are small and TIR optics can induce a high background, however, many studies have been limited to strong Raman scatterers or resonantly enhanced molecules.[17-18,23]

TIR Raman scattering at smooth metal films, SPR Raman spectroscopy

In light of the dependence of Raman scatter on the electric field amplitude encountered by analyte molecules, a clear solution to generating more Raman scatter from interfacial species is to increase the interfacial electric field strength. The inclusion of a smooth noble metal film at the interface, such as those used in surface plasmon resonance (SPR) spectroscopy, is one method to generate predictable and reproducible increased

interfacial electric fields through the excitation of surface plasmons (Figure 2b). Surface plasmons are charge density oscillations confined to the surface of a metal under appropriate excitation conditions.[24] The TIR geometry provides a method of coupling light waves to surface plasmons.

Surface plasmons can exist at an interface between a metal with permittivity $\varepsilon_m = \varepsilon'_m + i\varepsilon''_m$ and a dielectric with permittivity $\varepsilon_d = \varepsilon'_d + i\varepsilon''_d$ where ε' and ε'' represent the real and imaginary components of the permittivity, respectively and $\varepsilon'_m < -\varepsilon'_d$. In the visible and near-IR region of the spectrum; gold, silver, copper, aluminum and platinum have negative real components $\varepsilon'_m < 0$ and can support surface plasmons with most common dielectrics $\varepsilon'_d > 0$. With a proper metal / dielectric interface, surface plasmons can be excited by an evanescent wave in the TIR geometry by matching the parallel component of the incident light's wave vector to the propagation constant of the surface plasmon (*B)*. Only p-polarized incident light provides the appropriate matching condition and is used exclusively in this case. The condition for surface plasmon generation is:

$$\frac{2\pi}{\lambda}\eta_p \sin\theta_i = \mathrm{Re}\left[B\right] \tag{0.9}$$

where

$$B = \frac{2\pi}{\lambda}\left(\frac{\varepsilon_d \varepsilon_m}{\varepsilon_d + \varepsilon_m}\right)^{\frac{1}{2}} \tag{0.10}$$

λ is the excitation wavelength, η_p is the refractive index of the prism, and θ_i is the incident angle.[25] The electric field generated under these conditions is highest in intensity at the metal surface and decreases exponentially with increasing distance into the dielectric layer. As in

the TIR case, the penetration depth of the evanescent wave is defined as the depth where the electric field intensity drops to 1/e and can be calculated as:

$$d_{sp} = \frac{\lambda}{2\pi}\left(\frac{\varepsilon'_m + \varepsilon_d}{\varepsilon_d^2}\right)^{\frac{1}{2}} \tag{0.11}$$

The polarization of the evanescent electric field generated by surface plasmons is unique with the main component oscillating in the *z* direction with a minor contribution in the *x* direction (Figure 5b). Since s-polarized incident light cannot excite surface plasmons, p-polarized incident light is the only option for excitation of Raman scatter from analytes at the noble metal surface. This is in contrast to the case without the metal film where both s- and p- polarizations can be used.

The excitation of surface plasmons results in a sharp attenuation of the reflected light and can be calculated using Eq.1.8 and the complex refractive index of the metal (Figure 5a). The magnitude of the minimum correlates to the metal film thickness and mass changes at the interface. The angle of the minima, referred to as the SPR angle, depends on the refractive index within the sensing volume of the evanescent wave. When combined with Raman scattering, the location of the reflectivity minima corresponds to the angle where the maximum electric field is generated in the analyte layer and where the greatest magnitude of Raman scatter is predicted. The predicted electric field enhancement at a gold interface is on the order of 10^1 or 10^2 at the SPR angle compared to probing the same number of molecules with non-TIR illumination.

Raman scattering from surface plasmons has historically been accomplished using silver films since the predicted electric field enhancement is 2-3 times higher than predicted for a gold film.[26-29] Silver oxidizes readily, increasing the roughness of the metal surface that induces reproducibility issues in reflectivity and Raman measurements. Gold, on the other hand, provides a chemically stable support for surface plasmons, and is suitable for a wide variety of samples. Recent studies have used visible excitation to induce resonant Raman scatter from dye molecules on gold films at air and aqueous interfaces.[30] Near-IR excitation has an advantage over excitation with visible wavelengths when using gold films since the predicted electric field is roughly 2 times larger for the former. Chapter 3 summarizes instrument modifications necessary to obtain Raman spectra at smooth gold films and representative Raman spectra of analytes in air, aqueous, and concentrated environments. Raman spectra from a monolayer of non-resonant analytes are also demonstrated for the first time in this configuration.

TIR Raman spectroscopy at plasmon waveguides, (PWR) Raman spectroscopy

A second method of increasing the interfacial electric field encountered by an analyte in the TIR configuration involves the use of a plasmon waveguide resonator (PWR). A PWR consists of a thin series of stacked films capable of supporting guided modes and acts as an electric field amplifier. The PWR devices described in Chapter 4 consist of a thin gold film (≈ 50 nm) coated with a thicker (400-600 nm) dielectric coating (Figure 2c). In a PWR, both s- and p- polarized incident light can generate guided modes and generate an increased electric field at the waveguide / analyte interface. As mentioned previously, only p-polarized incident light can excite surface plasmons in a bare metal film under TIR. In the case of the

PWR, however, the dielectric coating on the film acts as a polarization converter and both p- and s- polarized incident light can be used to generate evanescent fields in the adjacent media with perpendicular polarizations.[31] The electric, E, and magnetic, M, field in a stratified medium with *s* layers can be calculated as:

$$\begin{bmatrix} E \\ M \end{bmatrix} = \prod_{j=1}^{s} \begin{bmatrix} \cos\beta_j & i(\sin\beta_j)/y_j \\ iy_j \sin\beta_j & \cos\beta_j \end{bmatrix} \begin{bmatrix} 1 \\ y_{j+1} \end{bmatrix} \tag{0.12}$$

with

$$\beta_j = 2\pi(\eta_j - ik_j)t_j \cos\theta_i / \lambda \tag{0.13}$$

and

$$y_j = \frac{(\eta_j - ik_j)}{\cos\theta_i} \tag{0.14}$$

where η_j and k_j are the real and imaginary refractive index components, and t_j is the thickness of layer *j*.[32] For a gold / silica waveguide, the largest electric field amplitudes are generated in the silica layer and the silica / analyte interface. Electric field enhancement at the analyte / waveguide interface is on the order of 10^2 (Figure 6b).

The reflected light from a PWR is very sharply attenuated at angles where the incident light resonates with guided modes in the film stack (Figure 6a). As a comparison, the FWHM of reflectivity minima with p-polarized incident light decreases roughly 6-fold from a bare gold film to a PWR.[33] Again, the reflected light from the interface is a valuable source of information, specifically in locating the required incident angles for coupling to guided modes.

PWR based devices were originally developed for use in SPR spectroscopy as substitutes for bare metal films.[32] The ability to generate resonance with both p- and s-polarized incident light added an additional spectroscopic dimension, and the decreased FWHM of reflectance spectra increased precision in comparison to SPR measurements at a bare gold film.[33] Additionally, the dielectric coating over the metal film acts as a protective shield to prevent damage to the metal surface. PWR spectroscopy is a relatively new technique that has had a significant impact in the biological sciences.[32] The primary use of PWR spectroscopy has been in the analysis of membrane phenomena where the parallel and perpendicular polarizations of the electric field in the analyte layer are particularly useful in monitoring membrane anisotropy during dynamic events.[31,33-36] Chapter 4 describes the application of plasmon waveguides to TIR Raman spectroscopy with 785 nm excitation and demonstrates Raman scattering from thin polymer films and aqueous analyte at a waveguide surface.

References

(1) Raman, C. V.; Krishnan, K. S. *Nature* **1928**, *121*, 501.

(2) Long, D. A. *Raman Spectroscopy*; McGraw-Hill International, 1977.

(3) McCreery, R. L. *Raman Spectroscopy for Chemical Analysis*; Wiley-Interscience, 2000; Vol. 157.

(4) Woods, D. A.; Bain, C. D. *Analyst (Cambridge, United Kingdom)* **2012**, *137*, 35.

(5) Greene, P. A.; Bain, C. D. *Spectroscopy Europe* **2004**, *16*, 8.

(6) D'Hooge, L.; Vigoureux, J. M.; Menu, C. *Journal of Chemical Physics* **1981**, *74*, 3639.

(7) Yoshikawa, M.; Gotoh, T.; Mori, Y.; Iwamoto, M.; Ishida, H. *Applied Physics Letters* **1994**, *64*, 2096.

(8) Ikeshoji, T.; Ono, Y.; Mizuno, T. *Applied Optics* **1973**, *12*, 2236.

(9) Iwamoto, R.; Ohta, K.; Miya, M.; Mima, S. *Applied Spectroscopy* **1981**, *35*, 584.

(10) Iwamoto, R.; Miya, M.; Ohta, K.; Mima, S. *Journal of Chemical Physics* **1981**, *74*, 4780.

(11) Beattie, D. A.; Larsson, M. L.; Holmgren, A. R. *Vibrational Spectroscopy* **2006**, *41*, 198.

(12) Fontaine, N. H.; Furtak, T. E. *Journal of the Optical Society of America B: Optical Physics* **1997**, *14*, 3342.

(13) Fontaine, N. H.; Furtak, T. E. *Physical Review B: Condensed Matter and Materials Physics* **1998**, *57*, 3807.

(14) Fujiwara, K.; Watarai, H. *Langmuir* **2003**, *19*, 2658.

(15) Greene, P. R.; Bain, C. D. *Colloids and Surfaces, B: Biointerfaces* **2005**, *45*, 174.

(16) Hoelzer, W.; Schroeter, O.; Richter, A. *J. Mol. Struct.* **1990**, *217*, 253.

(17) Nakanaga, T.; Takenaka, T. *Journal of Physical Chemistry* **1977**, *81*, 645.

(18) Takenaka, T.; Nakanaga, T. *Journal of Physical Chemistry* **1976**, *80*, 475.

(19) Tisinger, L. G.; Sommer, A. J. *MIcroscopy and Microanalysis* **2004**, *10*, 1318.

(20) Tyrode, E.; Rutland, M. W.; Bain, C. D. *Journal of the American Chemical Society* **2008**, *130*, 17434.

(21) Woods, D. A.; Petkov, J.; Bain, C. D. *Journal of Physical Chemistry B* **2011**, *115*, 7341.

(22) Woods, D. A.; Petkov, J.; Bain, C. D. *Journal of Physical Chemistry B* **2011**, *115*, 7353.

(23) Ishizaki, F.; Kim, M. *Japanese Journal of Applied Physics* **2008**, *47*, 1621.

(24) Raether, H. *Surface Plasmons on Smooth and Rough Surfaces and on Gratings*; Springer-Verlag: Berlin, 1988; Vol. 111.

(25) Homola, J. *Chemical Reviews* **2008**, *108*, 462.

(26) Pettinger, B.; Tadjeddine, A.; Kolb, D. M. *Chemical Physics Letters* **1979**, *66*, 544.

(27) Corn, R. M.; Philpott, M. R. *Surface plasmon-enhanced Raman scattering at thin silver films*, IBM Res. Lab., San Jose, CA, USA., 1983.

(28) Kurosawa, K.; Pierce, R. M.; Ushioda, S.; Hemminger, J. C. *Physical Review B: Condensed Matter and Materials Physics* **1986**, *33*, 789.

(29) Giergiel, J.; Reed, C. E.; Hemminger, J. C.; Ushioda, S. *Journal of Physical Chemistry* **1988**, *92*, 5357.

(30) Meyer, S. A.; Le Ru, E. C.; Etchegoin, P. G. *Analytical Chemistry (Washington, DC, United States)* **2011**, *83*, 2337.

(31) Abbas, A.; Linman, M. J.; Cheng, Q. *Biosensors and Bioelectronics* **2011**, *26*, 1815.

(32) Salamon, Z.; Macleod, H. M.; Tollin, G. *Biophysical Journal* **1997**, *73*, 2791.

(33) Abbas, A.; Linman, M. J.; Cheng, Q. *Sensors and Actuators B* **2011**, *156*, 169.

(34) Salamon, Z.; Brown, M. F.; Tollin, G. *Trends in Biochemical Sciences* **1999**, *24*, 213.

(35) Salamon, Z.; Tollin, G. *Spectroscopy* **2001**, *15*, 161.

(36) Hruby, V. J.; Alves, I.; Cowell, S.; Salamon, Z.; Tollin, G. *Life Sciences* **2010**, *86*, 569.

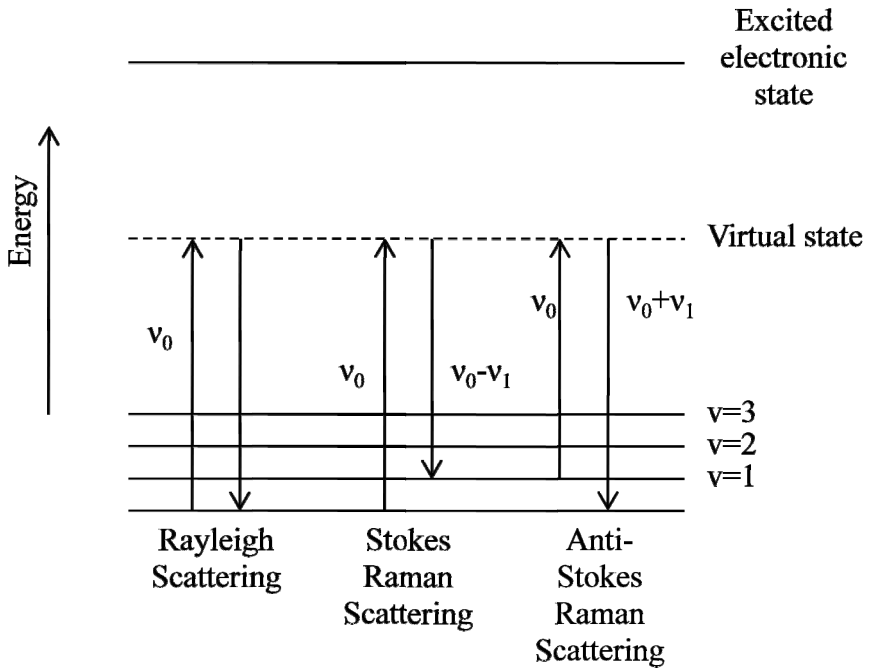

Figure 1: Spectroscopic transitions associated with Rayleigh and Raman scattering for vibrational levels v, where v_0 is the frequency of incident light.

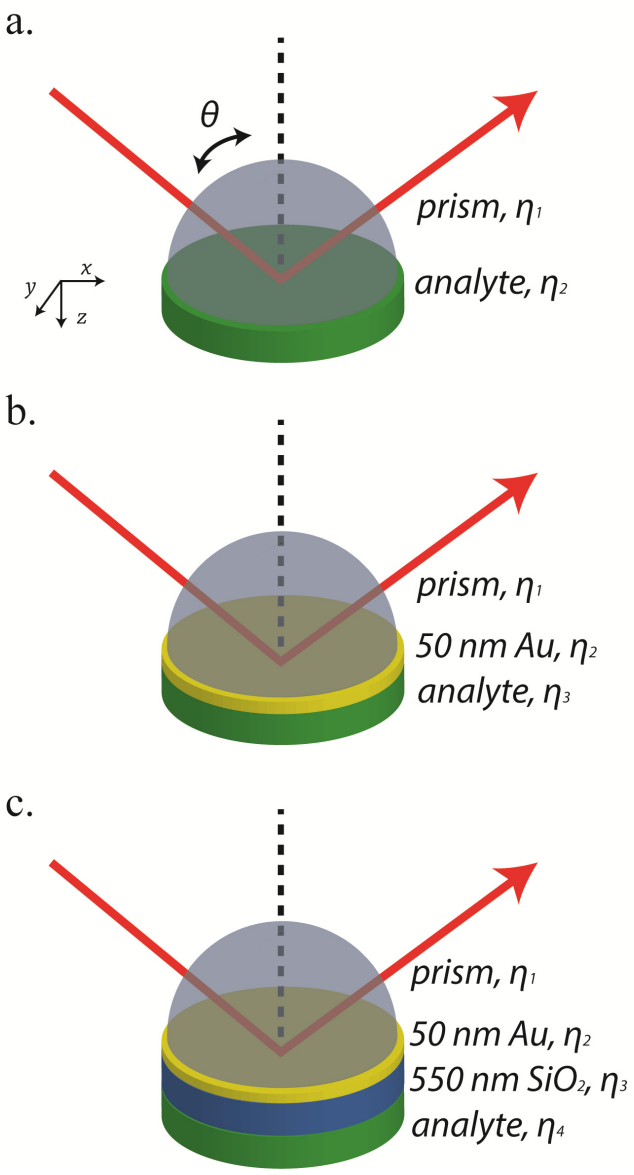

Figure 2: Experimental designs used in the Kretschmann configuration for (a) total internal reflection (TIR) Raman spectroscopy, (b) surface plasmon resonance (SPR) Raman spectroscopy, or (c) plasmon waveguide resonance (PWR) Raman spectroscopy.

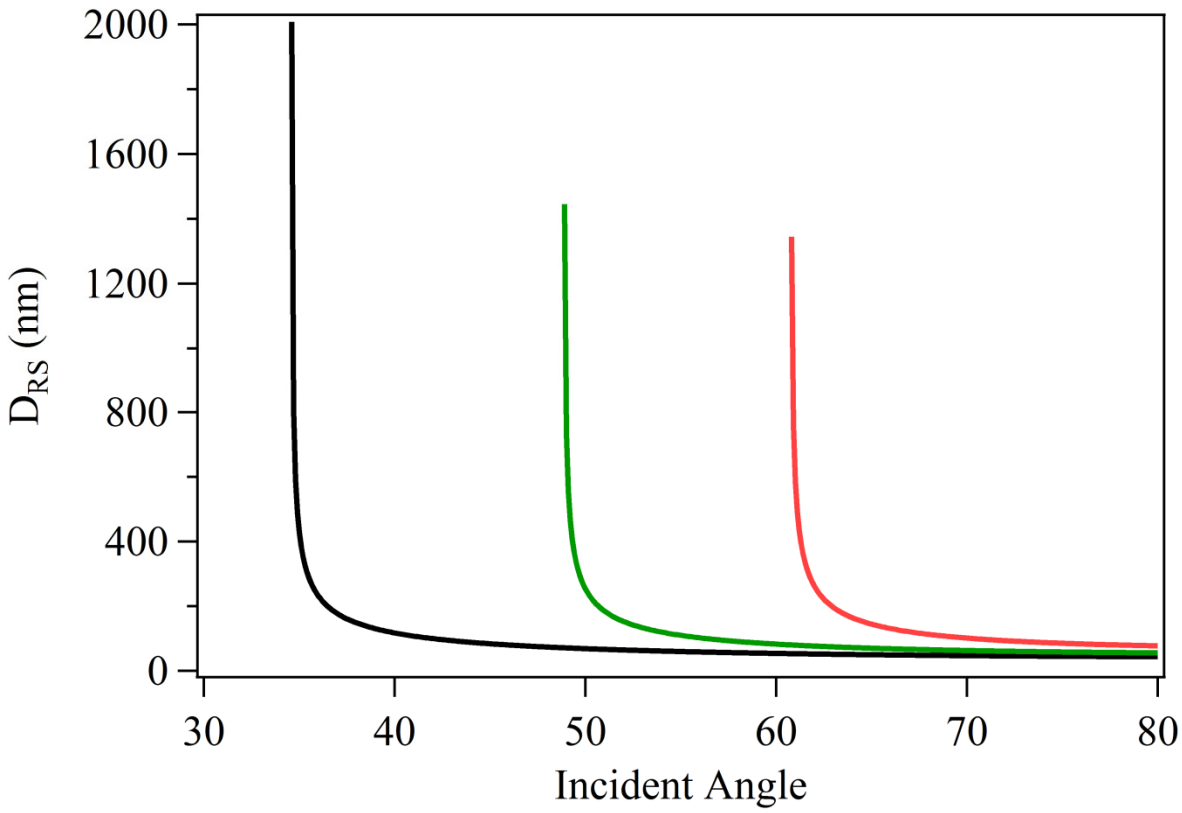

Figure 3: The depth Raman scatter is collected over (D_{RS}) as a function of incident angle when excited by an evanescent wave in the TIR configuration using a sapphire (η = 1.762) prism at an air (η = 1.00) (black), water (η = 1.327) (green), or organic (η = 1.537) (red) interface with 785 nm excitation.

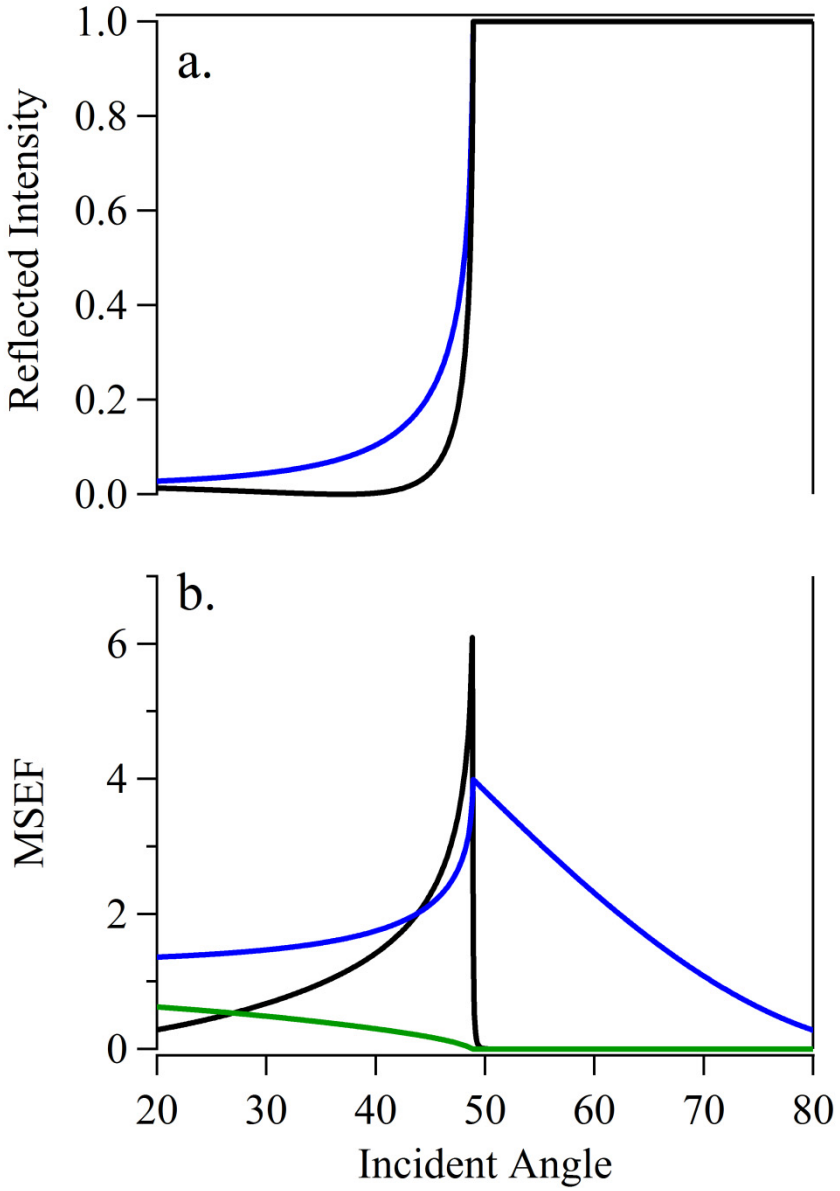

Figure 4: Results of Fresnel calculations for the reflected light intensity from a sapphire / water interface (a) for s-polarized (blue) and p-polarized (black) incident light at 785 nm and the corresponding mean-squared electric field (MSEF) relative to the incident electric field (b) in the *x* (green), *y* (blue) or *z* (black) planes.

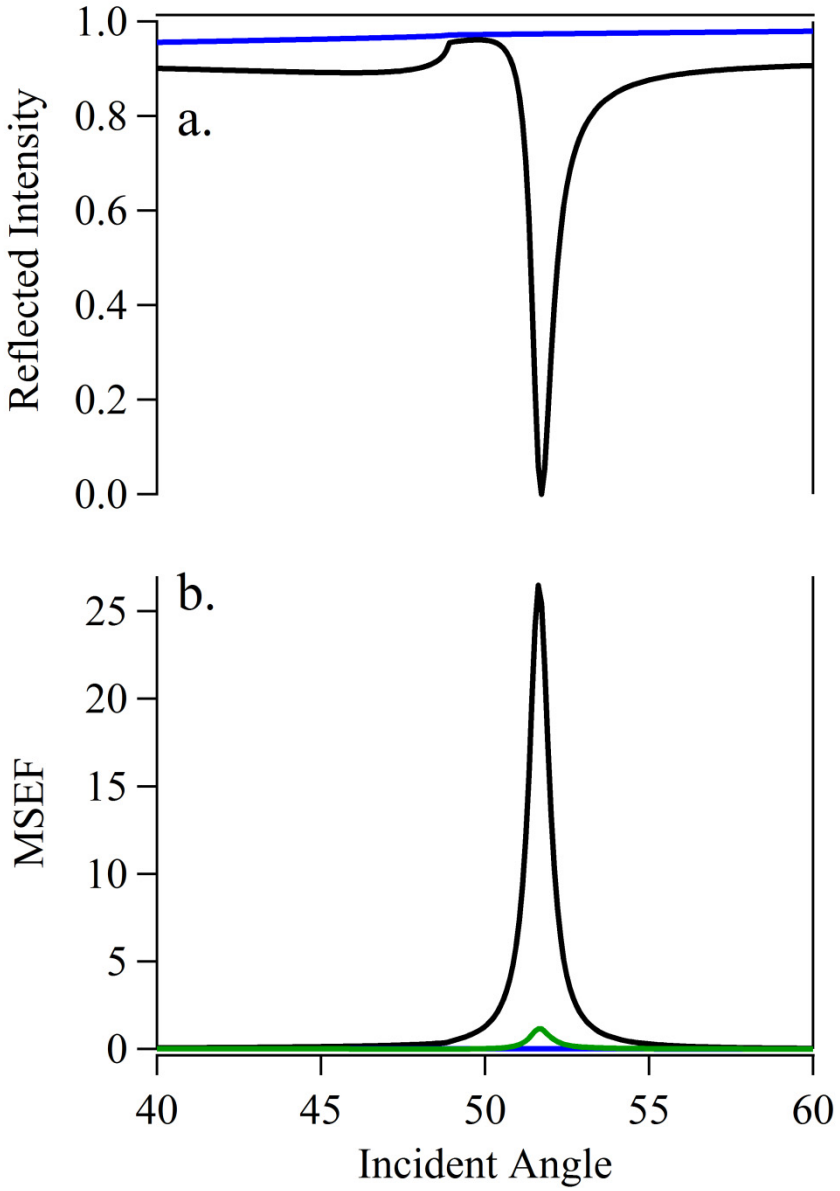

Figure 5: Results of Fresnel calculations for the reflected light intensity from a sapphire / 50 nm gold / water interface (a) for s-polarized (blue) and p-polarized (black) incident light at 785 nm and the corresponding mean-squared electric field (MSEF) relative to the incident electric field (b) in the *x* (green), *y* (blue) or *z* (black) planes.

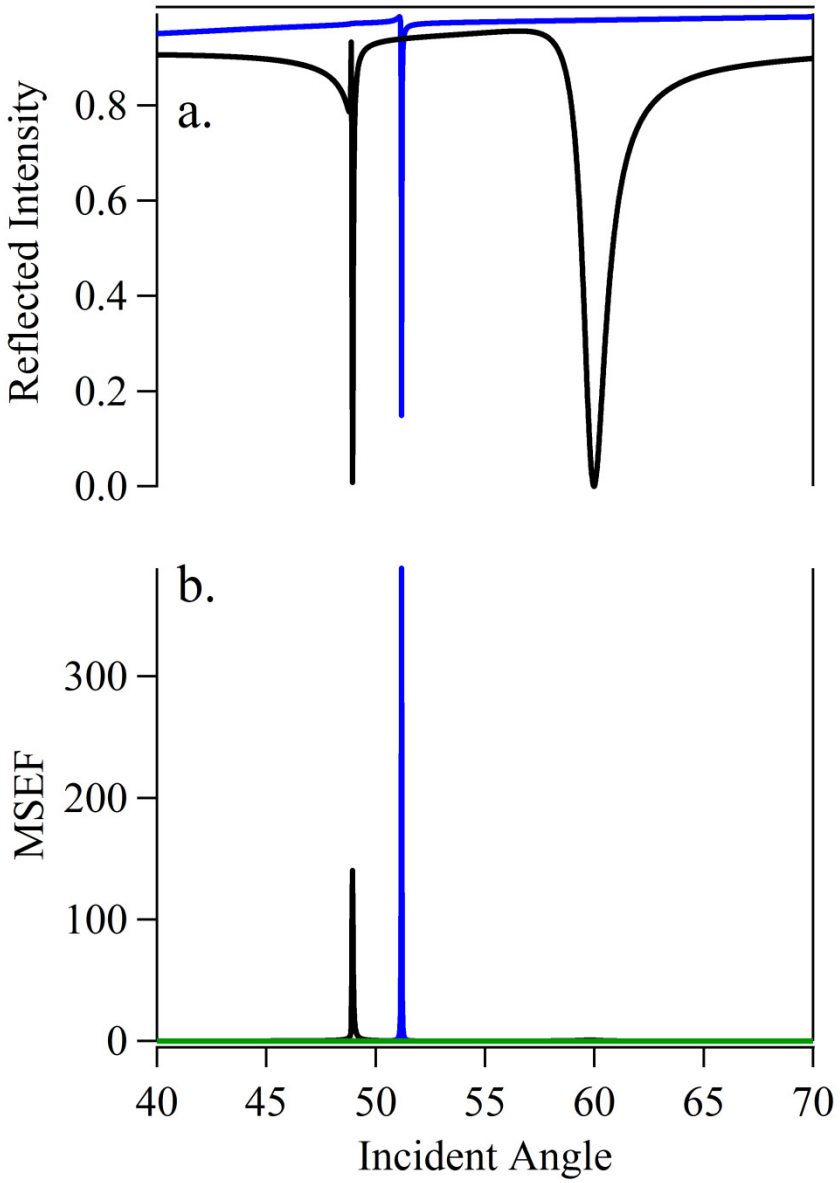

Figure 6: Results of Fresnel calculations for the reflected light intensity from a sapphire / 50nm gold / 550 nm silica / water interface (a) for s-polarized (blue) and p-polarized (black) incident light at 785 nm and the corresponding mean-squared electric field (MSEF) relative to the incident electric field (b) in the *x* (green), *y* (blue) or *z* (black) planes.

CHAPTER 2: DEVELOPMENT OF A SCANNING ANGLE TOTAL INTERNAL REFLECTION RAMAN SPECTROMETER

A paper published in Review of Scientific Instruments. 81, 043106 (2010)

Kristopher J. McKee and Emily A. Smith

Ames Laboratory, U. S. Department of Energy, Ames, Iowa 50011-3111, and Department of Chemistry, Iowa State University, Ames, Iowa 50011-3111

Abstract

A scanning angle total internal reflection (SA TIR) Raman spectrometer has been developed for measuring interfacial phenomena with chemical specificity and high axial resolution perpendicular to the interface. The instrument platform is an inverted optical microscope with added automated variable-angle optics to control the angle of an incident laser on a prism/sample interface. These optics include two motorized translation stages, the first containing a focusing lens and the second, a variable angle galvanometer mirror. The movement of all instrument components is coordinated to ensure that the same sample

location and area are probed at each angle. At angles greater than the critical angle, an evanescent wave capable of producing Raman scatter is generated in the sample. The Raman scatter is collected by a microscope objective and directed to a dispersive spectrometer and charged coupled device (CCD) detector. In addition to the collected Raman scatter, light reflected from the prism/sample interface is collected to provide calibration parameters that enable modeling the distance over which the Raman scatter is collected for depth profiling measurements. The developed instrument has an incident angle range of 25.5° to 75.5°, with a 0.05° angle resolution. Raman scatter can be collected from a ZnSe/organic interface over a range of roughly 35 to 180 nm. Far from the critical angle, the achieved axial resolution perpendicular to the focal plane is approximately 34 nm. This is roughly a 30-fold improvement relative to confocal Raman microscopy.

I. Introduction

A. Background

Total internal reflection (TIR) or attenuated total reflectance (ATR) Raman spectroscopy was first demonstrated as a surface sensitive vibrational technique by Ikeshoji in 1973.[1] Since its first validation, TIR Raman spectroscopy has been used to analyze a limited number of interfacial species at liquid-liquid, liquid-solid, and solid-solid interfaces.[2-8] The majority of these studies used a fixed angle of incident radiation; thus, collecting Raman scatter over a fixed distance from the interface. Typically, these distances range from 40 nm to 1 μm from the interface, depending on the instrument configuration employed.[4, 5] A number of reports have shown the surface sensitivity of the TIR Raman technique in the

analysis of polymer films and laminates of varying thickness.[5-8] Additionally, Bain and co-workers have analyzed a variety of samples including wax layers on plant leaves, boundary lubricants at frictional contacts, phospholipid bilayers, and adsorbed species at a silica/water interface.[8-10] There are a few reports where TIR Raman spectra have been measured using manual adjustment of the incident angle. For example, it has been shown that varying the angle of incident light at the sample interface can be used to measure the anisotropic refractive indices for nonlinear optical materials by determining the angle where maximum Raman scatter was collected.[11] Additionally, variable angle TIR Raman spectroscopy has been used to collect spectra of homogenous solutions and polymer laminates.[12-14] Up to now, the full scope of TIR Raman spectroscopy has not been utilized to perform high axial resolution depth profiling measurements. These measurements can be performed at ambient laboratory conditions, without obtrusive scanning probes, and will provide chemical specific information. Numerous materials science and biological applications will benefit from these measurements, including studies of interfacial multilayers and biological films

B. Theory

An in-depth treatment of the theory of Raman scattering from evanescent waves is available in the literature.[15] Briefly, total internal reflection occurs when light impinges on an interface between two materials of differing refractive indices, η_{prism} and η_{sample}, provided η_{prism} is greater than η_{sample} and the incident angle of light is greater than or equal to the critical angle, as determined by Snell's law. Under total internal reflection, there is no net flux of photons across the interface; however, an evanescent wave is generated in the lower index of refraction medium as a result of the electromagnetic boundary conditions.[16] The

evanescent wave travels parallel to the interface with a magnitude that decreases exponentially away from the interface. The depth at which the magnitude of the evanescent wave decreases to 1/e is known as the depth of penetration of the evanescent wave, d_p. Since incoherent scattering is proportional to the square of the electric field, Raman scatter generated by an evanescent wave drops off twice as fast as the electric field. As a consequence, more than 98% of the Raman scatter is generated at a distance less than $d_p/2$.[8] The depth over which Raman scatter can be collected, D_{RS}, is calculated from the excitation wavelength (λ), refractive indices of the prism (η_{prism}) and sample (η_{sample}), and the angle of incidence (θ) using equation 1.

$$D_{RS} = \frac{\lambda}{4\pi}\left(\left(\eta_{prism}{}^2 \sin^2\theta\right) - \eta_{sample}{}^2\right)^{-\frac{1}{2}} \qquad (1)$$

As denoted in equation 1, it is possible to adjust the depth over which Raman scatter is collected by varying the angle of the incident light on the prism/sample interface. If a ZnSe prism is coupled to an organic solution and the incident angle can be controlled in 0.05° increments, spectra could theoretically be collected for a change in D_{RS} of 1 nm. Comparing this to confocal Raman microscopy, where the resolution obtained in the axis perpendicular to the focal plane is approximately 1000 nm,[17, 18] several orders of magnitude improvement in the axial resolution is possible using TIR Raman spectroscopy.

The reflected light from a prism/sample interface can be modeled using Fresnel equations. For incident radiation of known polarization, the total reflected radiation, R_T, can be computed using equation 2. The fractions of the s- and p-polarized components of the

laser are x_s and x_p; and the quantity of reflected s- and p-polarized radiation from the interface are R_s and R_p, respectively.

$$R_T = \frac{x_s R_s + x_p R_p}{2} \qquad (2)$$

II. Experimental

A. Instrument Set-up

A schematic of the scanning angle TIR Raman microscope is shown in Figure 1. A 63mW 785 nm fiber coupled diode laser (Newport RLC785-63-50) fitted with a beam collimator is used as the excitation source. The beam is directed vertically with the use of a mirror oriented 45° relative to the plane of the optical table to a focusing lens mounted on a motorized 450 mm translation stage (Zaber Technologies) and then a variable angle galvanometer (Cambridge Technology Model 6231) mounted on a second 300 mm motorized translation stage. Both translation stages are mounted vertically with their direction of travel perpendicular to the plane of the optical table. The movement of the translation stages, which have 0.5 μm resolution, and the galvanometer, which has 0.04° angular resolution, are controlled with an in-house developed application for LabVIEW 8.6 with a National Instruments I/O DAQ board (NI USB-6221). Coordinating the movement of the two translation stages provides a constant optical path length between the focusing lens (L) and the prism/sample interface, and enables a facile match of the beam size and the microscope objective's field of view. The movement and focal length of the focusing lens can be changed depending on the desired laser spot size at the prism/sample interface. For all experiments, a 50.8 mm plano-convex lens with a focal length of 400 mm was used to

provide a 1.1 mm diameter laser spot size at the sample. The galvanometer mirror directs the beam onto a 25.4 mm diameter hemispherical ZnSe CVD prism ($\eta = 2.527$ at 785 nm) (ISP Optics), which is mounted in a custom sample holder on the stage of an inverted optical microscope (Nikon TE2000-U).

The mounted vertical position of the translation stages on adjustable steel mounts can be altered to vary the achieved scanning incident angle range. For these experiments, the stages were mounted to provide an available incident angle range of 25.5° to 75.5°. This incident angle range ensures that measurements could be taken below and above the critical angle for a variety of prism/sample interfaces. For example, if using a ZnSe prism, it would be possible to probe samples having a refractive index in the range of approximately 1.2 to 2.4.

Alignment of the laser spot at the prism/sample interface is aided by the use of a 12.5 mm CMOS camera mounted at the front port of the microscope. Using this camera, the position and area of the illuminated spot at the prism/sample interface are monitored at each angle. The generated Raman scatter is collected with a 10X, 0.22 NA objective lens (Nikon) and directed through the side port of the microscope where the light is focused onto an f/1.8i imaging spectrometer fitted with a holographic notch filter (Kaiser Optical Systems). Spectra are collected on a thermoelectrically cooled, back illuminated, deep depletion CCD (Pixis 400BR, 1300x400 Princeton Instruments) controlled with the WinSpec software package. A photodiode (Thor Labs SM1PD1A) fitted with a 1.0 O.D. neutral density filter is mounted opposite of the galvanometer and is used to collect the light reflected from the prism/sample interface.

B. Sample Analysis

1. Liquid Sample

A liquid sample holder was custom-made from a 1.3 mm thick glass petri dish. A circle roughly 19 mm in diameter was removed from the bottom of the dish and a 25.4 mm #1 glass cover slip was bonded to the bottom of the dish with optical adhesive (NOA 81, Norland Products) to create a sample well. To allow unimpeded passage of the incident and reflected radiation, the sides of the petri dish were partially removed. A schematic of the sample configuration is shown in Figure 2. In order to assemble the sample holder, 600 µL of 99% benzonitrile (Acros Organics) was added to the sample well, and the prism was mounted above the sample ensuring that no air bubbles were trapped at the interface. The sample assembly was then mounted on the stage of the optical microscope with the prism and sample centered above the collection optics. At each incident angle, a reflectivity measurement was recorded and a Raman spectrum acquired with an acquisition time of 10 minutes.

2. Polymer Film

A polystyrene film was fabricated by drop coating 50 µL of a 20% (w/w) polystyrene (M_w 280,000, Sigma Aldrich)/toluene (Fisher Scientific) solution directly onto the flat side of the ZnSe hemispherical prism. The solution was then allowed to dry under vacuum for 8 hours. After the film dried, the prism was inverted and placed onto a custom made aluminum plate, with a 12 mm diameter opening to accommodate the objective, mounted on the stage

of the microscope. Raman spectra were acquired at each angle with an acquisition time of 10 minutes.

C. Spectral Data Processing

All spectra were generated by averaging the central 100 vertical pixels of the CCD camera, where the horizontal direction is the spectral dimension. The data was exported to Grams AI (Thermo Scientific) and baseline corrected to eliminate the broad but low background signal from the instrument optics. The data was then exported to IgorPro 6 (Wavemetrics) for further analysis. The peak areas were determined using a Gaussian peak fitting algorithm. The reported data are the results for three replicate experiments. Algorithms were developed in IgorPro to fit the reflectivity and Raman data sets to models based on the Fresnel and D_{RS} calculations, as described in the following section.

III. Results and Discussion

A. Reflectivity Measurements

The computer controlled movement of the translation stages and galvanometer shown in Figure 1 can be used to vary the incident angle of the laser light on the prism/sample interface. The vertical displacement of the galvanometer and focusing lens are required to ensure the same area of the sample is being probed at each incident angle. The angle of incidence can be roughly measured using a protractor aligned on the microscope stage. However, further angle calibration is required for higher precision measurements. In order to calibrate the incident angle of the laser beam, the reflected light from a $ZnSe/H_2O$ interface

was recorded over a range of incident angles. This interface was chosen for angle calibration since the index of refraction of both materials is known at 785 nm, leaving the incident angle and laser polarization the only unknown parameters in equation 2. Using a laser power meter and a rotating polarizer, the measured laser polarization at the prism was 55% p- and 45% s-polarization. Shown in Figure 3A is the reflectivity data normalized to the highest measured reflected intensity and plotted along with theoretical reflectivity curves generated using equation 2. The instrument's incident angle measured using the microscope stage protractor does not match the calculated Fresnel values. After adjusting the data by -1.33°, a better match is achieved between the experimental and theoretical values (Figure 3B).

After calibrating the instrument's incident angle, there is still considerable disparity between experiment and theory (Figure 3B inset). As mentioned in the experimental section, the laser spot diameter at the interface was 1.1 mm. This large beam diameter ensures that a large area of the sample is being probed by the laser beam. It also enables the use of lower photon fluxes per unit area, and limits possible photodegradation of the sample. However, the fact that the beam is converging rather than collimated produces a distribution of incident angles at each instrument setting. The beam diameter was measured using a CMOS camera mounted at the front of the microscope to capture a visible image of the laser beam at the prism/sample interface allowing the range of angles probed to be back calculated. Using this measured diameter, the calculated incident angle spread is 2.9°. The beam diameter does not appreciably change as the instrument scans through the achievable incident angles.

If equation 2 is modified to account for an incident angle spread, $\delta\theta$, a good fit between experiment and theory is obtained (Figure 3C). The instrument's angular resolution

can be determined by varying the Fresnel fit to the higher and lower limit of the reflectivity data's standard deviation. The angular resolution of the instrument is 0.05° by this method.

The incident angle calibration and incident angle spread measured from the ZnSe/H_2O interface can be used to model the reflectivity data for interfaces where Raman scatter is to be collected. Prior to analyzing more complex samples, a model needs to be developed to correlate angle of incidence at the prism/sample interface with the depth over which Raman scatter is collected. A homogeneous solution of benzonitrile, a molecule with a high Raman scattering tensor, was chosen to develop this model. This model will have general applicability for other samples (e.g., polymer films, biofilms) provided the index of refraction of the sample is known from the literature, or concurrently measured with the Raman scatter using reflectivity data, as outlined below.

As with most samples of interest that will be measured with scanning angle TIR Raman spectroscopy, the index of refraction of benzonitrile at 785 nm is not available in the literature. However, this value can be determined from the ZnSe/benzonitrile reflectivity data. Shown in Figure 4 are the reflectivity values from a ZnSe/benzonitrile interface plotted along with a theoretical reflectivity curve accounting for the calibration parameters determined from the ZnSe/H_2O interface. To illustrate the effect of η_{sample} on the theoretical reflectivity curve, the resulting curves using η_{sample} equal to 1.492, 1.472, and 1.452 are shown in Figures 4A, 4B, and 4C, respectively. The refractive index of benzonitrile was determined to be 1.472 by minimizing the residual between the experimental and theoretical data (Figure 4B).

B. Raman Spectra

In contrast to TIR fluorescence measurements where the signal level is high, the choice of TIR prism is critical for low signal TIR Raman measurements. The background values obtained in the Raman spectra using a glass (SF11) prism were between 5.74 and 17.5 counts/sec throughout the fingerprint region of the spectrum (data not shown). The background included broad bands, likely due to fluorescence and scattering from the prism, with some minor contribution from other system optics. This background proved to be too high for practical TIR Raman measurements with this instrument. ZnSe, which has been used previously as in internal reflection element for ATR Infrared and Solid Immersion Lens Raman Microspectroscopy,[19] was found to produce the lowest background signal of the prisms tested, between 1.14 and 15.19 counts/sec, and was thus used for all subsequent Raman measurements. Additionally, the Raman spectrum of ZnSe only shows strong bands in the 200 to 500 cm^{-1} range, which do not interfere with the main Raman modes of benzonitrile or the commonly analyzed modes for most organic analytes.

Raman spectra of benzonitrile at a ZnSe interface were recorded at incident angles ranging from 32.67° to 66.67°. The critical angle for a ZnSe/benzonitrile interface using the previously determined refractive index for benzonitrile is 35.74°. The spectra are shown in Figure 5 for the most intense Raman peaks at select angles of incidence. The scattering intensity decreases as the incident angle increases further from the critical angle, as predicted by equation 1. The peak area at each incident angle was measured and is plotted in Figure 6 (right axis) for the 1000 cm^{-1} ring breathing mode, which is the most intense benzonitrile peak. Also plotted in the same graph are the calculated D_{RS} values using equation 1. Figure

6A shows there is good agreement between the D_{RS} values as calculated with equation 1 and the measured values. However, the high peak intensities that are predicted by equation 1 are not measured experimentally near the critical angle. As encountered with the Fresnel calculations, the D_{RS} equation must be modified to account for the converging excitation beam, which results in an incident angle spread rather than a single incident angle. To account for the angle spread, the δθ term is entered into equation 1 and the sum is taken over all angles, where x is a resolution parameter that describes the number of divisions in δθ. The equation for D_{RS} becomes:

$$D_{RS} = \frac{\sum_{i=-x}^{x} \frac{\lambda}{4\pi}\left(\eta_{prism}{}^{2}\sin^{2}\left(\theta+\left(\frac{\delta\theta}{2x}\right)i\right)-\eta_{sample}{}^{2}\right)^{-\frac{1}{2}}}{2x+1} \qquad (3)$$

As shown in Figure 6B, the modified D_{RS} equation with a 2.9° angle spread provides a good fit to the experimental data. It was found that an x value of 1000 provided sufficient resolution to model the data. This model explains why the predicted Raman signals are not measured near the critical angle, as predicted by equation 1 without an angle spread.

As confirmed in Figure 4B, the incident beam is not entirely under total internal reflection until the incident angle is above 37.20°. At this angle, the entirety of the beam is under total internal reflection conditions and will be referred to as tTIR for "total" total internal reflection. Spectra obtained at incident angles below tTIR will have some contribution from scattering caused by light transmitted through the ZnSe/benzonitrile interface (i.e., without surface sensitivity). The scatter from TIR cannot be differentiated from the scatter generated from the transmitted light; therefore, signal generated below the

tTIR angle is not useful for depth profiling, and is not modeled by equations 1 or 3. For the ZnSe/benzonitrile interface under total internal reflection conditions, the obtained Raman peak area can be correlated with the depth over which the Raman signal was collected using Figure 6B. For this interface and instrument settings, the D_{RS} versus incident angle curve is valid; however, the correlation of this curve to peak area will have to be performed for each peak in the Raman spectrum. This calibration is performed by fitting the experimentally determined peak area to the D_{RS} curve using a correlation factor that accounts for different scattering tensors for each Raman active mode.

The D_{RS} range achieved for the ZnSe/benzonitrile interface from tTIR to the highest incident angle spanned from 35 to 180 nm. The smallest measured change in D_{RS} was 5 nm between 58.67° and 66.67. This corresponds to a 0.9% change in Raman peak area. However, the average uncertainty in the Raman peak area was found to be 9.5%. This translates to a 34 nm uncertainty in measuring D_{RS}, which is the axial resolution at this interface. A smaller angle change closer to the tTIR value from 37.47° to 37.95° corresponds to a 40 nm change in D_{RS}, and a 22.4% change in the peak area. A summary of the measured instrument performance is provided in Table I.

As a preliminary demonstration of the instrument's capabilities for measuring SA TIR Raman spectra on a solid sample, spectra were collected at incident angles from 40.29° to 66.61° from a 56 ± 7 μm polystyrene film drop coated directly onto the prism. At these incident angles, the calculated D_{RS} values range from 37 to 190 nm. Figure 7 shows the correlation of the Raman peak areas for the 1001 cm^{-1} ring breathing mode to the calculated D_{RS} curve using Equation 3.

IV. Conclusions

To our knowledge, this is the first report of an automated scanning angle total internal reflection Raman spectrometer. The instrument and calibrations described herein provide the basis for chemical specific depth profile measurements at an interface with high axial resolution. Preliminary studies also show that, in addition to measurements in solution, the instrument is capable of collecting TIR Raman spectra from thin solid films. The large incident angle range that can be scanned with the current set-up, combined with the microscopy format, allow for the potential analysis of a multitude of liquid and solid samples. Current efforts are aimed to measure polymer laminate films and biofilms.

Acknowledgements

Work at the Ames Laboratory was supported by the Department of Energy-Basic Energy Sciences under Contract No. DE-AC02-07CH11358.

References

(1) T. Ikeshoji, Y. Ono, and T. Mizuno, Appl. Optics **12**, 2236 (1973).

(2) D.A. Beattie, M. L. Larsson, and A. R. Holmgren, Vib. Spectrosc. **41**, 198 (2006).

(3) K. Fujiwara, and H. Watarai, Langmuir **19**, 2658 (2003).

(4) P. R. Greene, and C. D. Bain, Colloid. Surface. B **45**, 174 (2005).

(5) L.G. Tisinger, and A. J. Sommer, Microsc. Microanal. **10**, 1318 (2004).

(6) R. Iwamoto, M. Miya, K. Ohta, and S. Mima, J. Am. Chem. Soc. **102**, 1212 (1980).

(7) R. Iwamoto, K. Ohta, M. Miya, and S. Mima, Appl. Spectrosc. **35**, 584 (1981).

(8) P. A. Greene, and C. D. Bain, Spectroscopy Europe **16**, 8 (2004).

(9) C. Lee, H. Wacklin, and C. D. Bain, Soft Matter **5**, 568 (2009).

(10) E. Tyrode, M. W. Rutland and C. D. Bain, J. Am. Chem. Soc. **130**, 17434 (2008).

(11) M. Yoshikawa, T. Gotoh, Y. Mori, M. Iwamoto, and H. Ishida, Appl. Phys. Lett. **64**, 2096 (1994).

(12) N. H. Fontaine, and T. E. Furtak, J. Opt. Soc. Am. B, **14**, 3342 (1997).

(13) N. H. Fontaine, and T. E. Furtak, Phys. Rev. B **57**, 3807 (1998).

(14) R. Iwamoto, M. Miya, K. Ohta, and S. Mima, J. Chem. Phys. **74**, 4780 (1981).

(15) L. D'Hooge, J. M. Vigoureux, and C. J. Menu, J. Chem. Phys. **74**, 3639 (1981).

(16) W. M. Reichert, P. A. Suci, J. T. Ives, and J. D. Andrade, Appl. Spectrosc. **41**, 503 (1987).

(17) N. Everall, Spectroscopy (Duluth, MN, United States) **19**, 22 (2004).

(18) N. Everall, Spectroscopy (Duluth, MN, United States) **19**, 16 (2004).

(19) A. F. Sohn, L. G. Tisinger, and A. J. Sommer, Microsc. Microanal. **10** (Suppl2), 1316 (2004).

Figures

Table I. SA TIR Raman instrument capabilities and measured performance for a ZnSe/benzonitrile interface.

Incident Angle Range	25.50° - 75.50°
Angular Resolution	0.05°
D_{RS} resolution	34 nm

	Angles	ΔD_{RS}	% change in Raman peak area
Close to tTIR	37.47° - 37.95°	40 nm	22.4%
Far from tTIR	58.67° - 66.67°	5 nm	0.9%

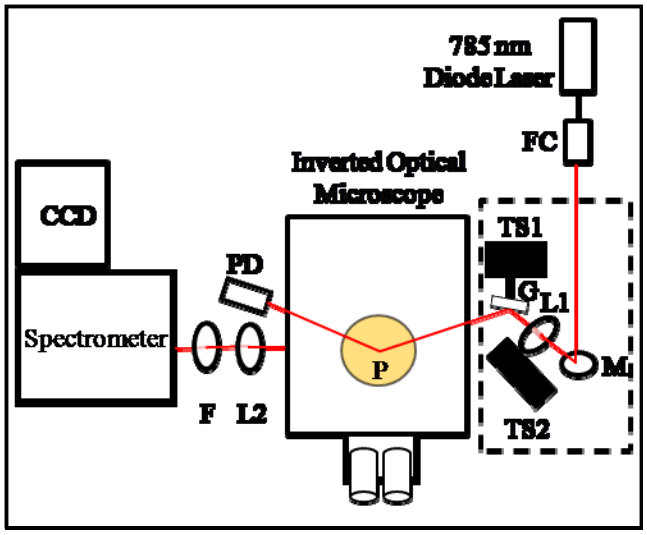

Figure 1. Schematic from the top of the scanning angle total internal reflection Raman microscope. The laser beam exits the fiber collimator (FC) and impinges on a mirror (M) oriented at a 45° to direct the beam vertically through a focusing lens (F) to the galvanometer mirror (G), both of which are mounted on motorized translation stages (TS). The galvanometer mirror directs the beam downward at an angle to the ZnSe prism (P)/sample interface. The light reflected from the interface is collected by a photodiode (PD) mounted on the opposite side of the prism. The Raman scatter generated in the sample is collected by a microscope objective and directed through a focusing lens (L) and a laser line filter (F) before entering the spectrometer equipped with a Near IR enhanced CCD. Optics in the dashed boxed are oriented perpendicular to the optical table, and have been offset for clarity.

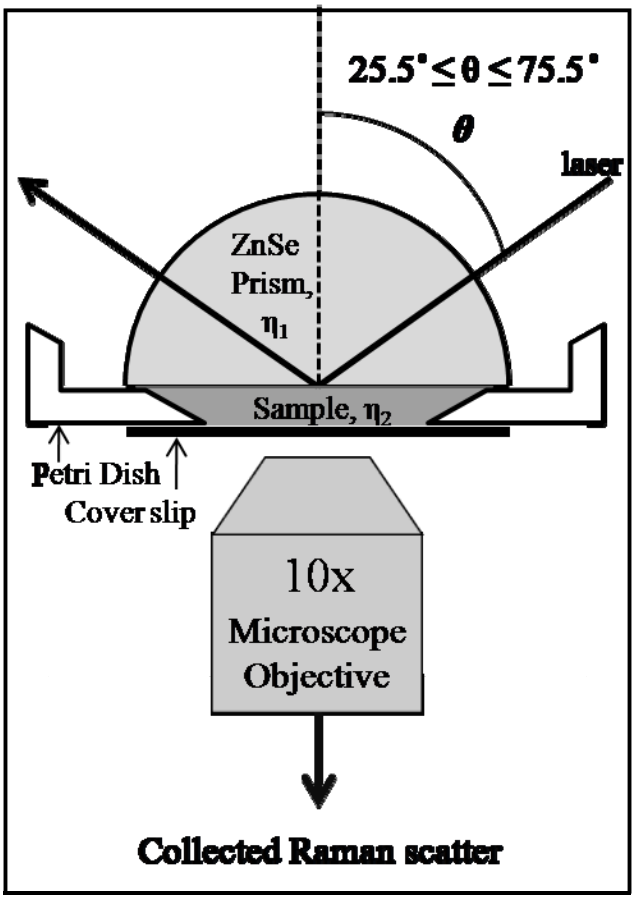

Figure 2. Schematic of the sample holder and total internal reflection illumination geometry. The Raman scatter generated by the evanescent wave is collected by a 10x, 0.22 NA microscope objective.

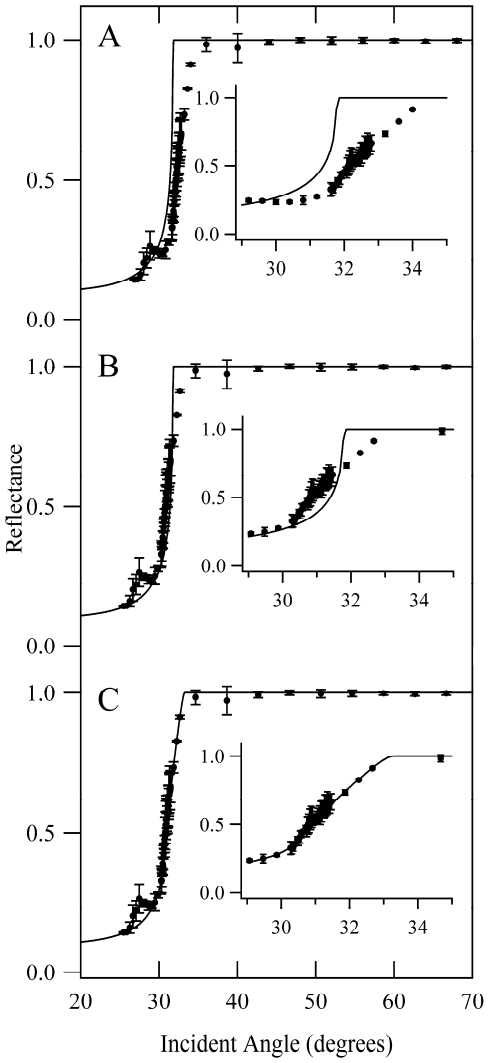

Figure 3. Reflectance curve obtained at a ZnSe/H_2O interface (circles) with a 55% s-polarized, 45% p-polarized 785 nm laser. The solid line is the theoretical reflectance curve calculated using a Fresnel equation (A) prior to adjusting the incident angle of the data set; (B) after adjusting the incident angle of the data set; and (C) after introducing an incident angle spread into the theoretical Fresnel equation. The insets show an expanded view near the critical angle.

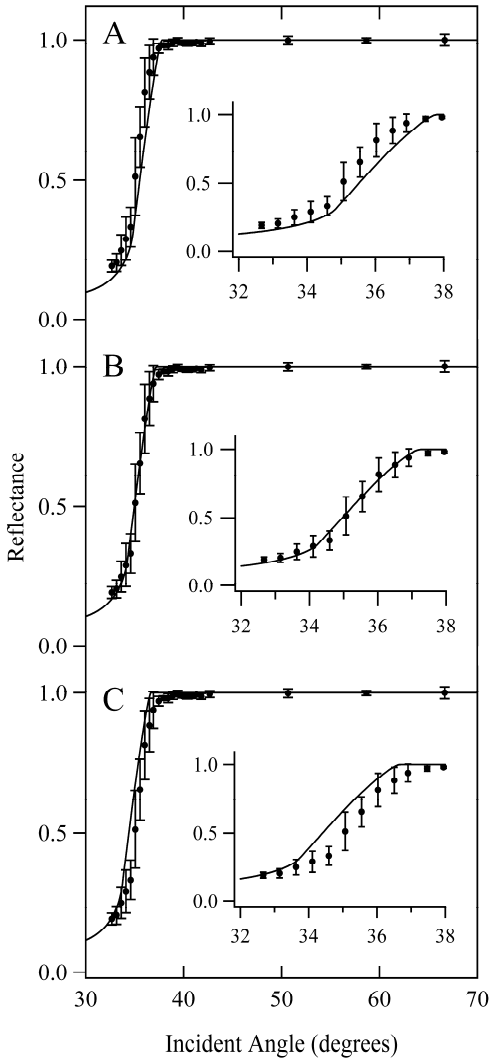

Figure 4. Reflectance curve for a ZnSe/benzonitrile interface after angle adjustments were made (circles) and theoretical reflectance curves (line) with 785 nm incident radiation and (A) η_{sample} = 1.492, (B) η_{sample} = 1.472, which was found to be the best fit, and (C) η_{sample} = 1.452. The insets show an expanded view below the critical angle.

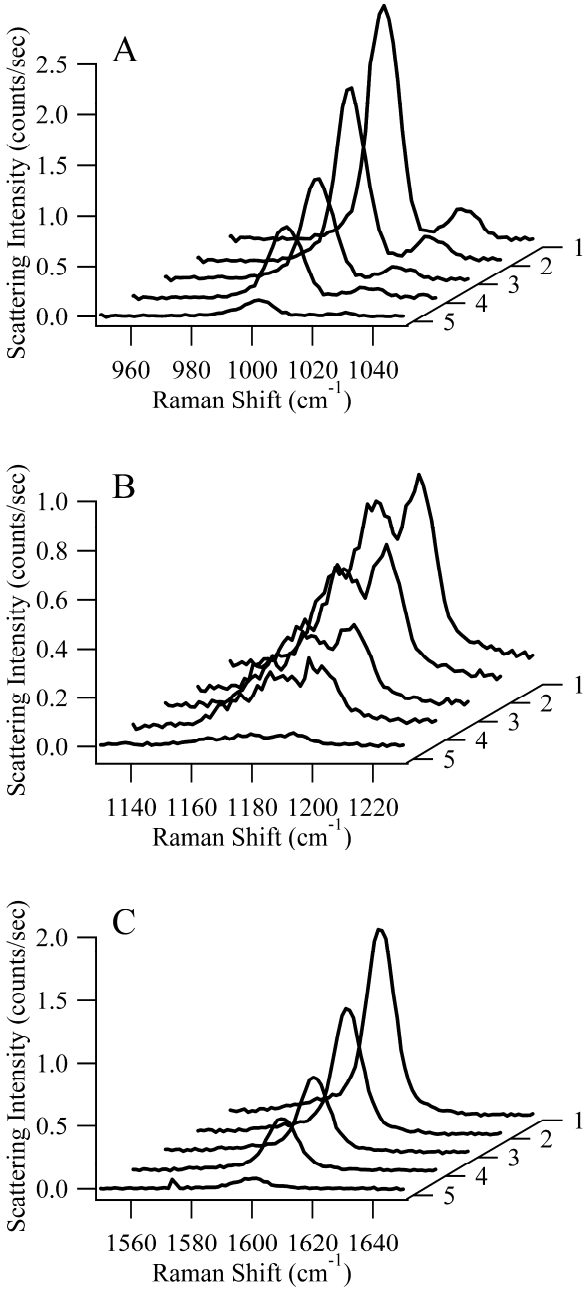

Figure 5. TIR Raman spectra of benzonitrile at varying incident angles from (A) 950 to 1050 cm^{-1}, (B) 1130 to 1230 cm^{-1}, and (C) 1550 to 1650 cm^{-1}. The corresponding incident angles are (1) 37.47°, (2) 38.43°, (3) 41.31°, (4) 42.67°, and (5) 58.67°.

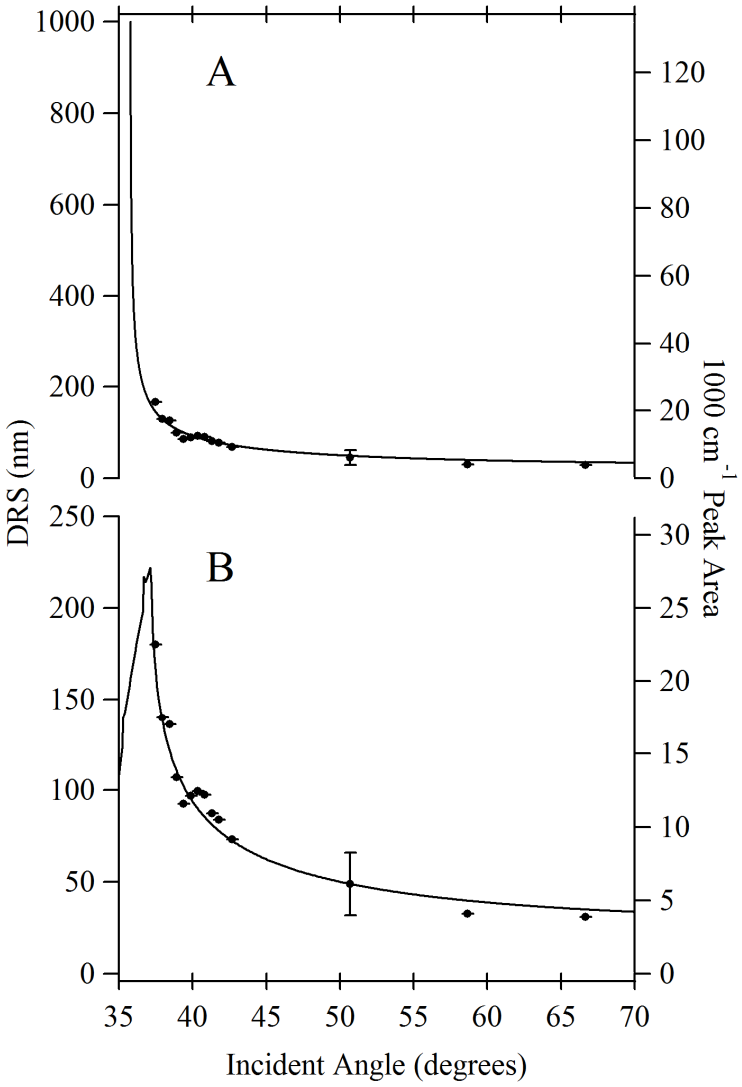

Figure 6. (Right axis) Raman peak areas (circles) for the 1000 cm^{-1} benzonitrile peak , and (left axis) D_{RS} curves (line) with (A) no angle spread, and (B) ±1.45° angle spread above and below the indicated x-axis value. The indicated error bar is the average uncertainty in peak area measured for all incident angles.

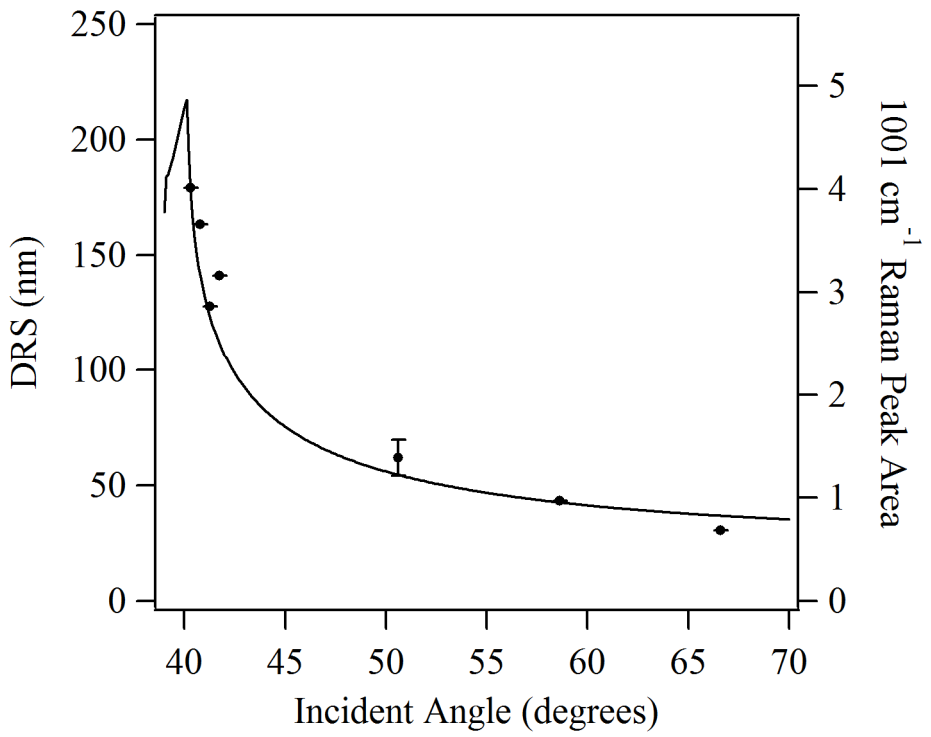

Figure 7. (Right axis) Raman peak areas (circles) for the 1001 cm^{-1} polystyrene peak, and (left axis) D_{RS} curves (line) with ±1.45° angle spread above and below the indicated x-axis value. The indicated error bar is the average uncertainty in peak area measured for all incident angles.

CHAPTER 3: NEAR IR SCANNING ANGLE TOTAL INTERNAL REFLECTION RAMAN SPECTROSCOPY AT SMOOTH GOLD FILMS

A paper published in Analytical Chemistry. 84, 4300 (2012)

Kristopher J. McKee, Matthew W. Meyer, and Emily A. Smith

The Ames Laboratory, U.S. Department of Energy, and Department of Chemistry, Iowa State University, Ames, Iowa 50011-3111.

Abstract

Total internal reflection (TIR) Raman and reflectivity spectra were collected for non-resonant analytes as a function of incident angle at sapphire or sapphire/smooth 50 nm gold interfaces using 785 nm excitation. For both interfaces, the Raman signal as a function of incident angle is well-modeled by the calculated interfacial mean square electric field (MSEF) relative to the incident field times the thickness of the layer being probed in the Raman measurement (D_{RS}). The Raman scatter was reproducibly enhanced at the interface containing a gold film relative to the sapphire interface by a factor of 4.3 to 4.6 for aqueous pyridine or 2.2 to 3.7 for neat nitrobenzene, depending on the analyzed vibrational mode. The mechanism for the increased Raman signal is the enhanced MSEF at incident angles

where propagating surface plasmons are excited in the metal film. The background from the TIR prism was reduced by 89 to 95% with the addition of the gold film, and the percent relative uncertainty in peak area was reduced from 15 to 1.7% for the 1347 cm^{-1} mode of nitrobenzene. Single monolayers of benzenethiol (S/N = 6.8) and 4-mercaptopyridine (S/N = 16.5) on gold films were measured by TIR Raman spectroscopy with 785 nm excitation (210 mW) without resonant enhancement in 1 minute.

Introduction

Total internal reflection (TIR) Raman spectroscopy is a surface sensitive technique that provides information about the chemical content at an interface.[1-12] In a typical TIR experiment, the illuminating light is directed onto an interface between a high refractive index prism or objective and a lower index of refraction sample at an incident angle at or higher than the critical angle. Under TIR, the Raman signal is confined to the interface as a result of the generated evanescent wave's limited penetration into the sample. The depth over which the Raman scatter is generated (D_{RS}) depends on the incident angle of the illuminating light, the wavelength of light and the indices of refraction of the interfacial species ($\eta_{prism}/\eta_{sample}$). D_{RS} is one half the penetration depth of the evanescent wave and typically ranges from a hundred nanometers to a couple of microns.[13-14] The number of Raman scatterers generating the signal is related to D_{RS} for a homogenous sample.

Raman cross sections are smaller than most fluorescence cross sections, and fewer molecules are probed in the TIR geometry compared to non-TIR illumination. High backgrounds generated in the TIR prism also remain problematic for many TIR Raman measurements.[15-16] As a result, TIR Raman spectra often have low S/N ratios, despite the TIR

geometry theoretically providing modest signal enhancement relative to non-TIR illumination when the same number of molecules are probed. With 785 nm excitation at a sapphire/sample interface, the increase in the electric field at the critical angle is calculated to be between ~5x (η_{sample} = 1.57) or ~7x (η_{sample} = 1.33) the incident electric field. The majority of TIR Raman studies use visible excitation sources, and monolayer detection is possible using a high laser power (e.g., 1 W) and large incident angles to decrease D_{RS}. Near-IR excitation is preferred for applications where high background from fluorescent compounds may be present or where photodegradation is a concern, such is the case for many biological samples. With near-IR excitation, however, TIR Raman signal at large incident angles is low even for molecules with large Raman cross-sections due to the ν^4 dependence of Raman scatter and several minute acquisition times have been required.[16] To decrease overall analysis time, increasing the signal from small probe depths with near-IR excitation is required.

Common enhancement strategies for linear Raman spectroscopy are surface enhanced Raman spectroscopy (SERS),[17-18] resonance Raman spectroscopy (RRS),[19-20] or in combination surface enhanced resonance Raman spectroscopy (SERRS).[21] These enhancement techniques have limitations that reduce their broad applicability.[22] SERS requires an analyte interaction with a nanoparticle or roughened noble metal surface and reproducibility is poor in most SERS experiments. Nanofabricated SERS substrates have increased the reproducibility of SERS measurements significantly however intra- and inter-substrate signal differences remain a focus of current research.[23] TIR Raman, in contrast to SERS, provides enhanced interfacial Raman signals that extend further than a couple of nanometers from the substrate, which may be beneficial for some applications. For example

enhanced SERS signals are limited to molecules, biomolecules, and thin polymers at the surface whereas TIR Raman can be used to measure polymer layers several hundred nanometers thick.[16] One key issue is that the SERS signal is not easily modeled, limiting the ability to obtain quantitative measurements. For resonance Raman spectroscopy, the analyte must have an electronic transition that coincides with the energy of the excitation source. To date, many TIR Raman studies have utilized the resonance Raman effect.

An alternative approach to enhance Raman signals under TIR is to use smooth metal substrates at the interface, akin to those used in surface plasmon resonance (SPR) spectroscopy.[24-31] Hereafter this is referred to as SPR Raman spectroscopy. Gold is the most commonly used metal for SPR spectroscopies due to its chemical stability and optical properties in the visible and near-IR region of the spectrum. The largest MSEF is generated at the gold/sample interface at the SPR angle. This is the angle with the greatest attenuation of the reflected light intensity and is associated with the excitation of surface plasmon polaritons. Recently, 633 and 647 nm excitation wavelengths were used to measure the resonant Raman scatter from Nile blue at sapphire/50 nm gold/water and glass/50 nm gold/air interfaces, respectively.[30] The predicted MSEF enhancement at a gold interface is on the order of 10^1 or 10^2 at the SPR angle compared to non-TIR illumination Raman measurements, and the MSEF enhancement is ~2x larger for near-IR versus visible excitation wavelengths due to gold's smaller real and larger imaginary refractive index components in the near-IR. While the expected signal enhancement with SPR Raman is smaller than many values reported for SERS, the signal is predicted to be both reproducible and well-modeled by Fresnel calculations.[32] Additionally, SPR Raman measurements probe deeper into the interface than SERS allowing SPR Raman measurements of thicker films (~100 nm).

Until recently,[30] SPR Raman measurements have primarily used Ag films in the Kretschmann configuration.[33-34] The predicted enhancement using a Ag film is ~2x larger than predicted for a gold film using near-IR excitation and ~3x larger using visible excitation. Ag films, however, are not chemically stable, which increases surface roughness and makes the SPR Raman data irreproducible and difficult to model. Smooth gold films provide a stable substrate for reproducible signal enhancement.

The goals of this work are to measure the TIR Raman scatter for neat and aqueous non-resonant analytes at a smooth gold film with near-IR excitation; to compare the Raman scatter generated at gold and sapphire interfaces; to model the Raman signal obtained at different incident angles, and to demonstrate a monolayer of analyte can be measured by non-resonant SPR Raman spectroscopy. The work presented herein will provide a method for reproducible non-resonant TIR Raman signal enhancement with near-IR excitation, and information to generate a fundamental understanding of other plasmon enhanced Raman scattering techniques.

Materials and Methods

Chemicals.

Nitrobenzene, benzenethiol, 4-mercaptopyridine (Sigma-Aldrich, St. Louis, MO) and pyridine (Fisher Scientific, Waltham, MA) were used as received. 1.25 M Pyridine was prepared in deionized water from an 18.2 MΩ EasyPure II filtration system.

Instrumentation.

All experiments were performed using a previously reported scanning angle TIR Raman microscope that was further modified as outlined below and in the Supplemental

Figure S1.[16] The s-polarized output from a 785 nm 0.5 W single frequency laser (Toptica Photonics XTRA HP) was directed through an OD 0.4 neutral density filter before it was directed vertically to a focusing lens and a variable angle mirror mounted on separate motorized translation stages with the direction of travel perpendicular to the plane of the optical table. The variable angle mirror directs the now p-polarized excitation beam to the prism/sample interface that is centered on the stage of an inverted wide-field optical microscope. A 1280x1024 CMOS camera (Thor Laboratories DCC1545) mounted in the front port of the microscope is used to align the laser onto the center of the prism. The intensity of the reflected beam from the prism/sample interface is measured using a 1 cm^2 photodiode (Thor Laboratories FDS1010) fitted with a OD 1.4 neutral density filter and mounted on a third vertically oriented motorized translation stage opposite the variable angle mirror. The Raman scatter generated at the prism/sample interface is collected with a 10x 0.30 NA objective lens and focused from the side port of the microscope to an f/1.8i imaging spectrometer (Kaiser Optical Systems) fitted with a 1340x400 near-infrared enhanced CCD detector (Princeton Instruments Pixis 400BR). The movement of the translation stages and variable angle mirror are controlled through an in-house developed program with LABVIEW 8.6.

The excitation power at the sample was 210 mW and all Raman spectra were collected by binning 160 vertical pixels (i.e. the non-spectral dimension) on the CCD with an integration time of 60 seconds, unless otherwise noted. The intensity of the reflected light from a sapphire/water interface was collected to calibrate the instrument's incident angle and to measure the incident angle spread as previously reported.[16] These parameters are extracted from the reflectivity data through modeling with Fresnel calculations,[35] and are required to

model the Raman signal at varying incident angles. For the instrument used in these studies, the incident angle spread varies from ±0.25 to ±0.50 degrees. Replicate measurements were acquired by making consecutive scans through the entire angle range required for a particular interface and the gold films used were from a single batch deposition either on sapphire or SF-11 glass.

Peak areas and intensities for the measured Raman modes were calculated by fitting them to Gaussian curves with the "Multipeak fitting 2" algorithm in IGOR Pro 6. The reflected light intensity from the interface was modeled with Fresnel calculations using macros developed in IGOR Pro 6 that allow the incident angle spread to be varied.[16] Fresnel calculations were also used to calculate mean square electric fields at the interface.[32,35] Signal-to-noise ratios were calculated as the maximum peak intensity after background subtraction divided by the standard deviation of the noise measured in a 50 cm^{-1} region of the spectrum where no analyte peaks were present. The percent relative uncertainty in peak area is reported as the standard deviation divided by the mean peak area.

Sample Configuration.

A custom-made flow cell was designed for the Kretschmann configuration. For TIR Raman measurements, a 25.4 mm diameter hemispherical sapphire prism (ISP Optics) was pressed to a 25.4 mm dia. x 400 μm sapphire disc ensuring optical contact with index matching fluid (n_D = 1.7800 Cargille Labs, Cedar Grove, NJ). The sapphire disc composed the top of the flow cell under which the analyte solution was introduced through channels in a KEL-F disc using a syringe. For SPR Raman measurements, the sapphire or SF-11 disc was coated on one side with 2 nm Cr followed by 47 nm gold (Evaporated Metal Films Corporation, Ithaca, NY for films on sapphire or GWC Technologies, Madison, WI for films

on SF-11). The RMS roughness of the gold films was 0.639 nm measured by atomic force microscopy (Supplemental Figure S2). The sapphire discs and prisms were cleaned by immersion in piranha etch (5:1 H_2SO_4:H_2O_2) to remove organic residues, rinsed with deionized water and dried with N_2. [Caution: Piranha etch is aggressive and explosive. Never mix piranha waste with organic solvents. Check precautions before using it.] The flow cell was cleaned by sonication in aqueous Alconox® detergent and ethanol, then dried with N_2 before each experiment.

Results and Discussion

TIR Raman Spectra at a Sapphire Interface.

Figure 1A and B illustrate the dependence of D_{RS} and MSEF on the incident angle at the sapphire/1.25 M pyridine or sapphire/nitrobenzene interface, respectively. The critical angle for the sapphire/nitrobenzene interface is 61.2 degrees. At this angle both D_{RS} (578 nm) and the MSEF (5.3) are at a maximum, so Raman scatter is predicted to be the largest at the critical angle. Compared to the nitrobenzene interface, the sapphire/1.25 M pyridine interface is associated with a slightly higher MSEF of 6.9 and D_{RS} of 693 nm at the 49.9 degree critical angle. As expected, the largest signal for all Raman peaks is measured at the critical angle for both interfaces (Figure 1C and 1D).

Spectra obtained near the critical angle or using non-TIR illumination, referred to hereafter as the bulk spectra, for pyridine and nitrobenzene are shown in Figure 2A and 2B. In all cases, the Raman spectra were collected using p-polarized incident light, and the spectra were normalized to the 1003 (pyridine) or 1347 (nitrobenzene) cm^{-1} peak in the spectrum in order to make relative intensity comparisons. Several differences are observed

between the bulk and TIR Raman spectra. Sapphire prisms can be used in TIR Raman spectroscopy with near-IR excitation to limit spectral background. Despite the overall low background compared to other prism materials, intense peaks at 643 and 748 cm^{-1} are observed in the TIR Raman spectra obtained at the sapphire interface. There are also changes in peak intensities under TIR compared to the bulk spectra. The nitrobenzene ν_{8a}, ν_{8b}, ν_{9a}, ν_{9b} and ν_{6b} (Wilson Notation, spectral assignments shown in Supplemental Information Table S1) in plane modes are relatively more intense in the TIR compared to the bulk spectrum. The predominate peaks in the pyridine TIR spectrum with higher relative intensities compared to the bulk are the ν_{9a}, ν_{8b} and ν_{8a} modes. In all cases, these peaks are non-totally symmetric modes characterized by large depolarization ratios. The electric field generated under TIR is enhanced in the Z direction, perpendicular to the interface, and to a minor extent in the X direction, parallel to the interface with p-polarized incident light. Depolarized Raman scatter is more efficiently collected than polarized Raman scatter in this case, which explains the measured differences in peak intensity.

The MSEF at the interface depends on the sample index of refraction (η_{sample}) and this parameter must be known in order to model the Raman data at varying incident angles. The reflected light from the sapphire/sample interface is simultaneously collected with the Raman scatter to measure $\eta_{sample,\ 785\ nm}$ (Figure 3, top panel). Fresnel calculations model the reflectivity data for 1.25 M pyridine in water or neat nitrobenzene and the refractive indices were experimentally determined to be 1.344 or 1.537, respectively.

The Raman peak area for the ν_1 (pyridine) and NO_2 symmetric stretch (nitrobenzene) are plotted in Figure 3 (bottom panel, right axis) along with the respective MSEF x D_{RS} curve (left axis). The peak area axis is multiplied by a constant value in order to account for

differences in Raman cross sections, bulk concentrations and collection efficiencies, which are not accounted for in the MSEF x D_{RS} model. Within the uncertainty of the measurements, the MSEF x D_{RS} curves model the Raman peak area at both interfaces. Compared to the sapphire/organic interface, the MSEF x D_{RS} curve has a higher intensity near the critical angle at the sapphire/water interface. This is the result of a larger electric field at the interface with increasing disparity between the prism and sample refractive indices, and as a result of the smaller angle spread at lower incident angles. In general, the uncertainties in the Raman peak area for the 1.25 M pyridine solution are larger than those measured for nitrobenzene since fewer pyridine molecules are within the probed area. This results in a lower S/N ratio for the pyridine spectra: 63 (pyridine) vs. 132 (nitrobenzene) for the most intense peak in the spectrum at an incident angle near the respective critical angle. In a previous report, the Raman peak area from a ZnSe/benzonitrile interface was modeled by the D_{RS} curve without consideration of the MSEF.[16] Since the MSEF does not significantly change over the studied incident angle range for the bare prism interface, the D_{RS} curve provides an acceptable fit to the Raman peak area.

SPR Raman Spectra at a Gold Interface.

At the sapphire/gold/nitrobenzene or sapphire/gold/1.25 M pyridine interface, the shape of the MSEF x D_{RS} curve is determined by the MSEF term (Figure 4A and 4B). The MSEF curve shows a maximum value at an angle larger than the critical angle, which is the predicted SPR angle. The expected enhancement in the Raman signal relative to bulk measurements, assuming the same number of Raman scatters is probed, is 64x or 30x for the aqueous or organic interface, respectively.

In most cases the sapphire peaks can be observed in measurements at a gold interface, but their intensity decreases by 89 - 95% compared to the sapphire interface (Figure 2A and 2B). A more dramatic example of the reduction in the prism's contribution to the spectral background at a gold interface is evident using a SF-11 prism, which is a high index of refraction glass commonly used for SPR and TIR-fluorescence spectroscopies (Figure 2C). Large broad peaks across the fingerprint region in the SF-11 Raman spectrum, which is divided by 5 to appear on the same scale as the spectrum obtained at the gold film, obscure analyte bands and limit its use in TIR Raman spectroscopy. At the gold interface the prism background is significantly reduced and analyte peaks are evident. In this manner, thin gold films can be used to mask or reduce background signals from the prism material, which represents a significant challenge in most TIR Raman measurements.[15-16] Other than the reduced prism background, the TIR Raman and SPR Raman relative peak intensities are similar when the spectra are normalized to the most intense analyte peak in the spectrum (Figure 2). The low S/N ratio for the 1.25 M pyridine SPR Raman spectrum, as a result of the smaller 156 nm D_{RS} value at this interface, explains why some peaks appear in the TIR Raman spectrum but not the SPR Raman spectrum.

As expected, the largest Raman peak intensity is not obtained at the critical angle, rather at the predicted SPR angle for a gold/1.25 M pyridine (Figure 4C) or gold/nitrobenzene (Figure 4D) interface. The reflected light intensity from these interfaces show the expected attenuation at the SPR angle (Figure 5, top panel). The reflectivity data has been modeled by Fresnel calculations with the appropriate angle spread described above. In all cases the Fresnel calculations predict the location of the critical angle and the SPR angle to within 0.3 degrees.

The same Raman modes used to generate the data shown in Figure 3 were used to generate the data shown in Figure 5 (bottom panel) for 1.25 M pyridine and nitrobenzene at the gold interface. Near the SPR angle, the Raman peak area is approximately the mirror image of the SPR curve, and the maximum Raman peak area is measured at the SPR angle. Similar to the modeled reflectivity data, there is a decent fit between the experimental Raman peak area and the MSEF x D_{RS} curve. The similarity between the shape of the reflectivity curve and the Raman peak area curve suggests that measurements at interfaces where the reflectivity data can be modeled will result in Raman peak areas that can be modeled, and that the reflectivity data can be used to predict the collected Raman signal. Differences between the predicted Raman peak area and the measured Raman peak area are attributed to gold films with a thicker than desired (2 nm) Cr adhesion layer and possible contamination of the gold film during the deposition process.

Comparison of Raman Signals at Sapphire and Gold Interfaces. As a result of the larger MSEF, more Raman scatter is predicted at the gold/aqueous than at the gold/organic interface assuming the same number of scatterers are probed. The theoretical enhancement factors were ~11x (aqueous pyridine) and ~9x (nitrobenzene) at a gold film compared to the sapphire interface. Measured enhancements are indicated in Figure 6, which shows plots of the Raman peak intensity divided by the calculated D_{RS} for each incident angle. As expected, the TIR Raman signal is a relatively flat line since this data representation should mimic the MSEF curves shown in Figures 1 (sapphire interface) or 4 (gold interface). The increase in the SPR Raman signal with respect to the TIR Raman signal represents signal enhancement when the same number of Raman scatters are probed. The appreciably enhanced modes of pyridine are ν_1 and ν_{12} with enhancement factors of 4.6 and 4.3. The ν_{8a}, ν_{8b}, NO_2 symmetric

stretch, ν_1, and ν_{12} modes of nitrobenzene gave enhancements of 3.7, 2.2, 3.7, 2.4 and 2.8, respectively. Average uncertainties in the Raman peak areas at the gold interface are smaller than at the sapphire interface for: nitrobenzene's ν_{8a}, ν_{8b}, ν_1, ν_{12} modes and NO_2 symmetric stretch; and pyridine's ν_1 mode. Analysis of the spectra reveals that all of these peaks have S/N ratios greater than 21. For example, the percent relative uncertainty of nitrobenzene's 1347 cm^{-1} peak area decreases from 15% at sapphire to 1.7% at the gold interface. Uncertainties in Raman peak areas did not improve at the gold interface for modes with lower S/N ratios.

The measured Raman enhancement is 2.4-4.1x lower than expected at the gold film. Previous studies have indicated a 10x lower than expected enhancement for pyridine at an Ag electrode in a similar experimental configuration.[36] This may be due to a combination of sub-optimal gold films, small changes in the collection efficiency at different excitation angles, and the small increase in the background as surface plasmons are excited in the gold. Unlike typical SERS data, it has been shown that the SPR Raman signal is well-modeled. None of the spectra shown herein have been background subtracted nor baseline corrected.

SPR Raman Measurement of a Monolayer without Resonant Enhancement**.**

For SERS, the analyte must be adsorbed or very close to the metal surface and surface selection rules must be considered when interpreting the spectra; whereas, the SPR Raman signal is predominately from analyte that is not adsorbed to the metal. To test whether a monolayer of adsorbate could be measured using SPR Raman spectroscopy with 785 nm excitation, a monolayer of benzenethiol or 4-mercaptopyridine was prepared on a gold film and probed under TIR at the SPR angle. Figure 7 shows the SPR Raman signal for the sapphire/gold/benzenethiol monolayer/water or sapphire/gold/4-mercaptopyridine

monolayer/air interfaces. The acquisition times range from 1 to 3 minutes using an incident power of 210 mW. The S/N ratios for the spectra obtained in 1 minute are 6.8 and 16.3 for benzenethiol and 4-mercaptopyridine, respectively. A comparison of the integrated peak areas of the 1002 cm^{-1} mode of benzenethiol from a monolayer or neat benzenethiol solution reveals that roughly 2% of the signal comes from adsorbate at the SPR angle, when the difference between the mean square electric field at the aqueous or benzenethiol interface (a factor of 2.4x) is factored in (Supplemental Figure S3). In SERS, chemical enhancement results from interaction between the metal and adsorbate species. Since the adsorbed species contribute little to the overall SPR Raman signal, chemical enhancement is negligible in these measurements. These spectra reveal that the SPR Raman technique is suitable for monolayer measurements with near-IR excitation wavelengths where no resonant enhancement is expected.

Conclusions

The detection of a monolayer of non-resonant molecules at a gold film with near-IR excitation is a significant step toward the broader application of the SPR Raman method. Near-IR excitation and the use of gold films in the TIR configuration provides a lower background from system optics, an overall decrease in the uncertainty of most Raman peak intensities and monolayer level sensitivity. The use of other noble metals (e.g. Ag) with more favorable plasmonic properties in the near-IR could provide a larger MSEF at the metal/sample interface and lead to measurements of weak Raman scatterers including biological samples; however, the chemical stability of the Ag film needs to be considered.

Currently, additional methods to increase the MSEF at the interface without introducing surface roughness to the metal are being pursued.

ACKNOWLEDGMENT

This research is supported by the U.S. Department of Energy, Office of Basic Energy Sciences, Division of Chemical Sciences, Geosciences, and Biosciences through the Ames Laboratory. The Ames Laboratory is operated for the U.S. Department of Energy by Iowa State University under Contract No. DE-AC02-07CH11358.

REFERENCES

(1) Ikeshoji, T.; Ono, Y.; Mizuno, T. *Applied Optics* **1973**, *12*, 2236.

(2) Iwamoto, R.; Miya, M.; Ohta, K.; Mima, S. *Journal of the American Chemical Society* **1980**, *102*, 1212.

(3) Iwamoto, R.; Miya, M.; Ohta, K.; Mima, S. *Journal of Chemical Physics* **1981**, *74*, 4780.

(4) Iwamoto, R.; Ohta, K.; Miya, M.; Mima, S. *Applied Spectroscopy* **1981**, *35*, 584.

(5) Nakanaga, T.; Takenaka, T. *Journal of Physical Chemistry* **1977**, *81*, 645.

(6) Takenaka, T.; Nakanaga, T. *Journal of Physical Chemistry* **1976**, *80*, 475.

(7) Fontaine, N. H.; Furtak, T. E. *Journal of the Optical Society of America B: Optical Physics* **1997**, *14*, 3342.

(8) Fontaine, N. H.; Furtak, T. E. *Physical Review B: Condensed Matter and Materials Physics* **1998**, *57*, 3807.

(9) Fujiwara, K.; Watarai, H. *Langmuir* **2003**, *19*, 2658.

(10) Greene, P. A.; Bain, C. D. *Spectroscopy Europe* **2004**, *16*, 8.

(11) Greene, P. R.; Bain, C. D. *Colloids and Surfaces, B: Biointerfaces* **2005**, *45*, 174.

(12) Hoelzer, W.; Schroeter, O.; Richter, A. *Journal of Molecular Structure* **1990**, *217*, 253.

(13) D'Hooge, L.; Vigoureux, J. M.; Menu, C. *Journal of Chemical Physics* **1981**, *74*, 3639.

(14) Woods, D. A.; Bain, C. D. *Analyst (Cambridge, United Kingdom)* **2012**, *137*, 35.

(15) Woods, D. A.; Petkov, J.; Bain, C. D. *Colloids and Surfaces, A: Physicochemical and Engineering Aspects* **2011**, *391*, 10.

(16) McKee, K. J.; Smith, E. A. *Review of Scientific Instruments* **2010**, *81*.

(17) Camden, J. P.; Dieringer, J. A.; Zhao, J.; Van Duyne, R. P. *Accounts of Chemical Research* **2008**, *41*, 1653.

(18) Stiles, P. L.; Dieringer, J. A.; Shah, N. C.; Van Duyne, R. P. *Annual Review of Analytical Chemistry* **2008**, *1*, 601.

(19) Asher, S. A. *Analytical Chemistry* **1993**, *65*, 201A.

(20) Asher, S. A. *Analytical Chemistry* **1993**, *65*, 59A.

(21) Kim, H.; Kosuda, K. M.; Van Duyne, R. P.; Stair, P. C. *Chemical Society Reviews*, *39*, 4820.

(22) Larmour, I. A.; Graham, D. *Analyst (Cambridge, United Kingdom)* **2011**, *136*, 3831.

(23) Guicheteau, J.; Christesen, S.; Emge, D.; Wilcox, P.; Fountain, A. W., III *Applied Spectroscopy* **2011**, *65*, 144.

(24) Brioude, A.; Lequevre, F.; Mugnier, J.; Dumas, J.; Guiraud, G.; Plenet, J. C. *Journal of Applied Physics* **2000**, *88*, 6187.

(25) Corn, R. M.; Philpott, M. R. *Surface plasmon-enhanced Raman scattering at thin silver films*, IBM Res. Lab., San Jose, CA, USA., 1983.

(26) Futamata, M. *Applied Optics* **1997**, *36*, 364.

(27) Giergiel, J.; Reed, C. E.; Hemminger, J. C.; Ushioda, S. *Journal of Physical Chemistry* **1988**, *92*, 5357.

(28) Kurosawa, K.; Pierce, R. M.; Ushioda, S.; Hemminger, J. C. *Physical Review B: Condensed Matter and Materials Physics* **1986**, *33*, 789.

(29) Liu, Y.; Xu, S.-P.; Xuyang, X.; Zhao, B.; Xu, W.-Q. *Journal of Physical Chemistry Letters* **2011**, *2*, 2218.

(30) Meyer, S. A.; Le Ru, E. C.; Etchegoin, P. G. *Analytical Chemistry (Washington, DC, United States)* **2011**, *83*, 2337.

(31) Zerulla, D.; Isfort, G.; Kolbach, M.; Otto, A.; Schierbaum, K. *Electrochimica Acta* **2003**, *48*, 2943.

(32) Hansen, W. N. *J. Opt. Soc. Am.* **1968**, *58*, 380.

(33) Kretschmann, E.; Raether, H. *Zeitschrift fuer Naturforschung, Teil A: Astrophysik, Physik und Physikalische Chemie* **1968**, *23*, 2135.

(34) Raether, H. *Surface Plasmons on Smooth and Rough Surfaces and on Gratings*; Springer-Verlag: Berlin, 1988; Vol. 111.

(35) *Code for Fresnel calculations was generously made available by Prof. Robert Corn at http://corninfo.ps.uci.edu/calculations.html*.

(36) Pettinger, B.; Tadjeddine, A.; Kolb, D. M. *Chemical Physics Letters* **1979**, *66*, 544.

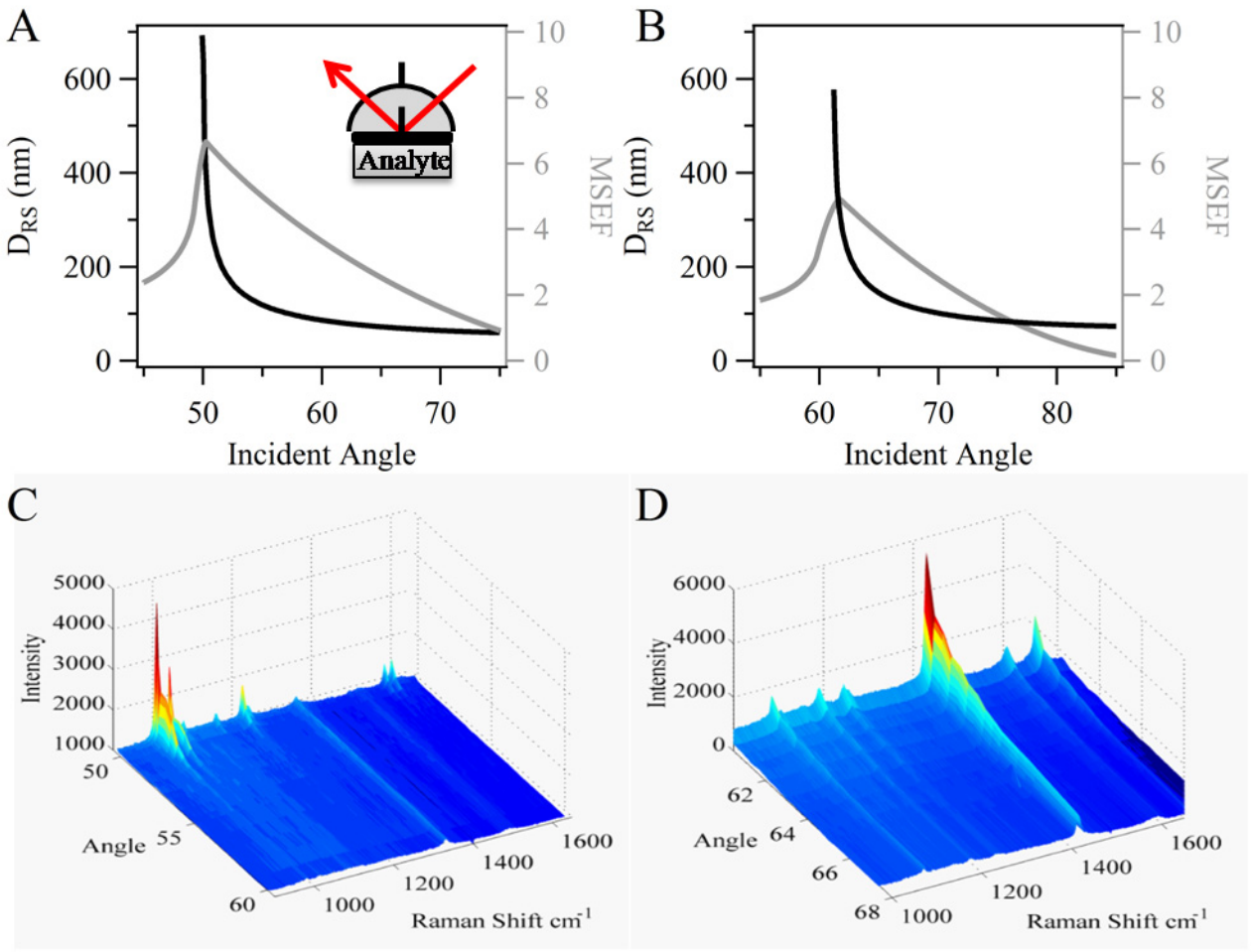

Figure 1. Calculated mean square electric field relative to the incident electric field (grey) and D_{RS} (black) for a (A) sapphire/1.25 M pyridine or (B) sapphire/nitrobenzene interface with a (A) ±0.25 or (B) ±0.50 degree incident angle spread. The measured Raman spectra of (C) 1.25 M pyridine or (D) nitrobenzene at a sapphire interface are shown at varying incident angles.

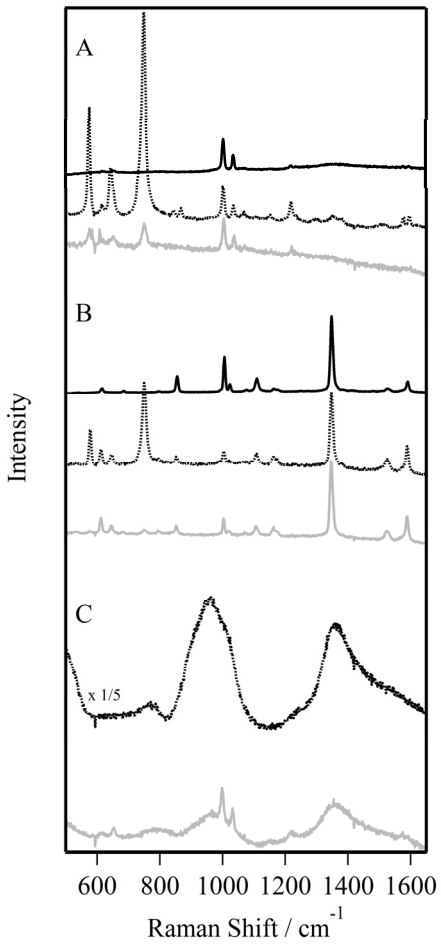

Figure 2. Bulk (black), TIR (black dotted), and SPR (grey) Raman spectra for (A) pyridine and (B) nitrobenzene normalized to the largest analyte peak in the spectrum. TIR Raman spectra were acquired near the critical angle. D_{RS} is 580 nm for pyridine and 414 nm for nitrobenzene. SPR Raman spectra were acquired at the SPR angle. D_{RS} is 156 nm for pyridine and 112 nm for nitrobenzene. Peaks at 643 and 748 cm^{-1} are assigned to sapphire. The spectra in A and B have been offset for clarity. TIR and SPR Raman spectra from 0.5 M pyridine (C) using a SF-11 prism at a 56 degree incident angle show a large decrease in the SF-11 background spectrum in the SPR-Raman configuration. The TIR spectrum is multiplied by 1/5 to appear on the same scale, the spectra have not been offset.

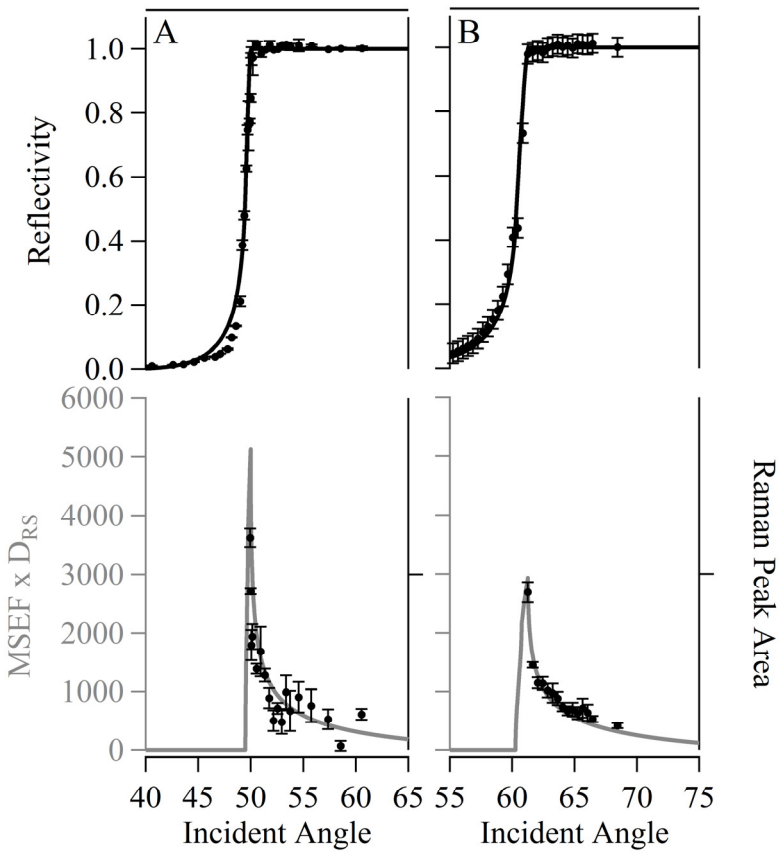

Figure 3. Reflected light intensity (top, symbol) and TIR Raman peak areas (bottom, symbol) for a (A)sapphire/1.25 M pyridine or (B) sapphire/nitrobenzene interface. The reflected light intensity is modeled using Fresnel calculations with a (A) ±0.25 or (B) ±0.50 degree incident angle spread (solid line). The Raman peak areas are modeled by the calculated MSEF times D_{RS} (solid line). Error bars represent standard deviation from 3 replicate measurements.

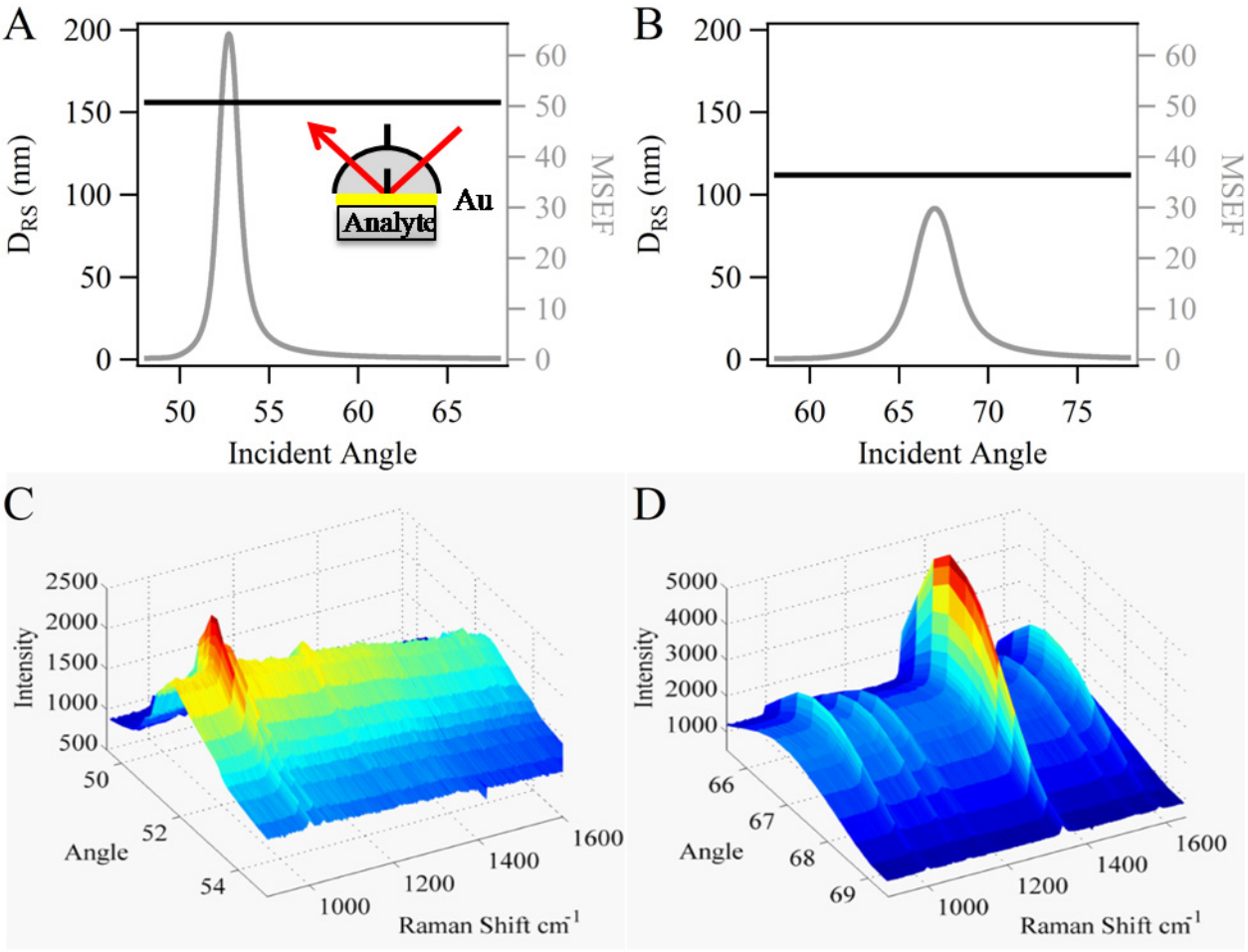

Figure 4. Calculated MSEF (grey) and D_{RS} (black) for a (A) sapphire/gold/1.25 M pyridine interface or (B) sapphire/gold/nitrobenzene interface with a (A) ±0.25 or (B) ±0.50 degree incident angle spread. The measured Raman spectra of (C) 1.25 M pyridine or (D) nitrobenzene at a sapphire/gold/analyte interface are shown from 50-55 and 65-70 degrees, respectively.

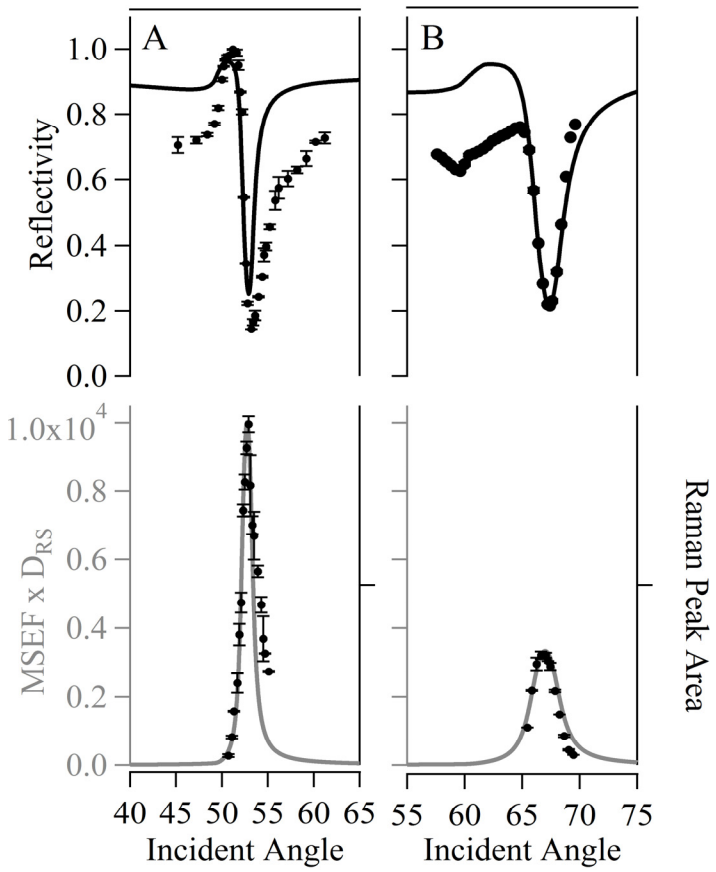

Figure 5. Reflected light intensity (top, symbol) and SPR Raman peak areas (bottom, symbol) for a (A) sapphire/gold/1.25 M pyridine or (B) sapphire/gold/nitrobenzene interface. The reflected light intensity is modeled using Fresnel calculations with a (A) ±0.25 or (B) ±0.50 degree incident angle spread (solid line). The Raman peak areas are modeled by the calculated MSEF times D_{RS} (solid line). Error bars represent standard deviation from 3 replicate measurements.

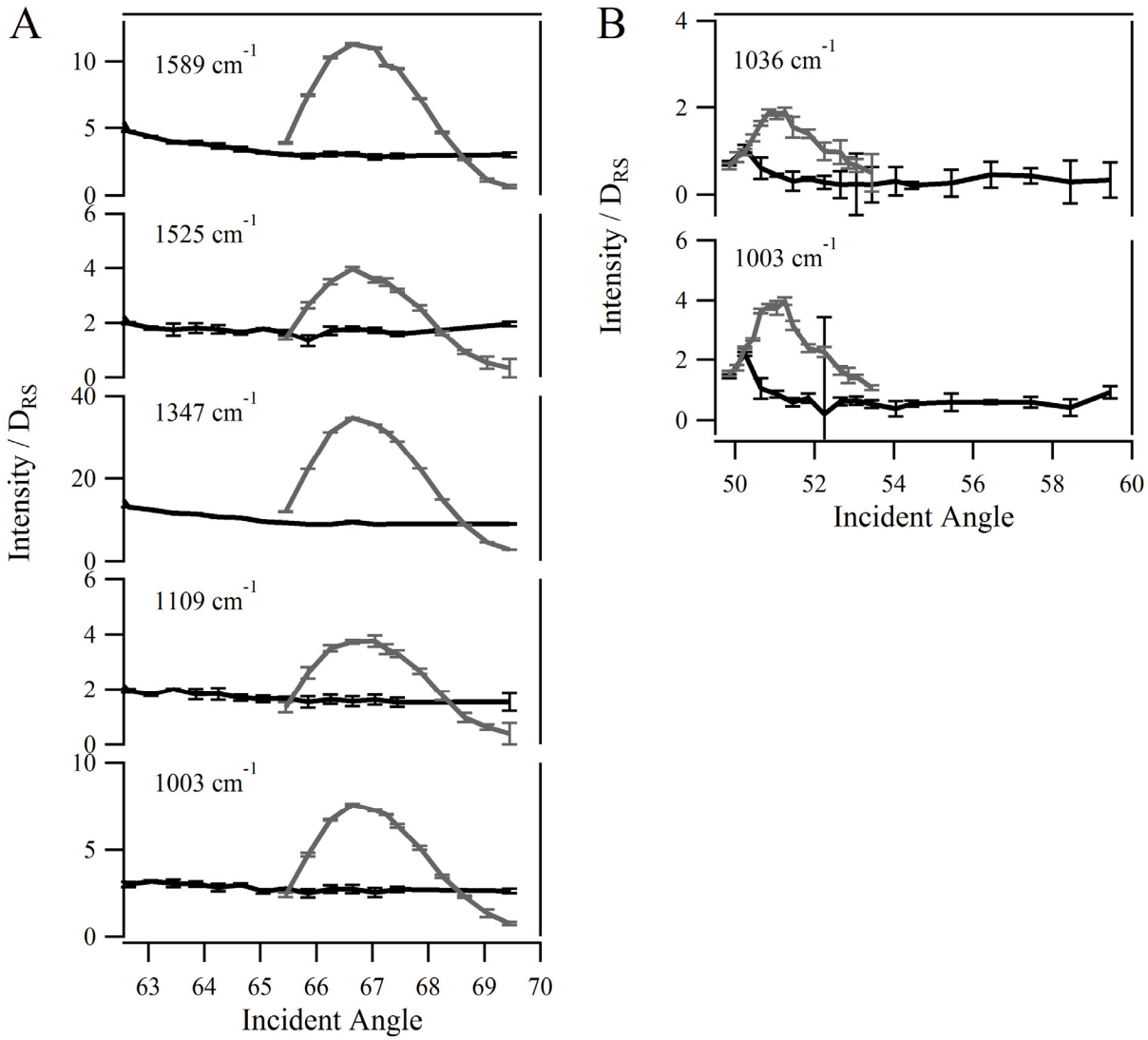

Figure 6. Raman peak intensities divided by D_{RS} for the indicated vibrational modes for TIR (black) or SPR (grey) Raman spectra with (A) nitrobenzene and (B) 1.25 M pyridine at different incident angles. The error bars represent the percent relative uncertainty calculated from 3 replicate measurements.

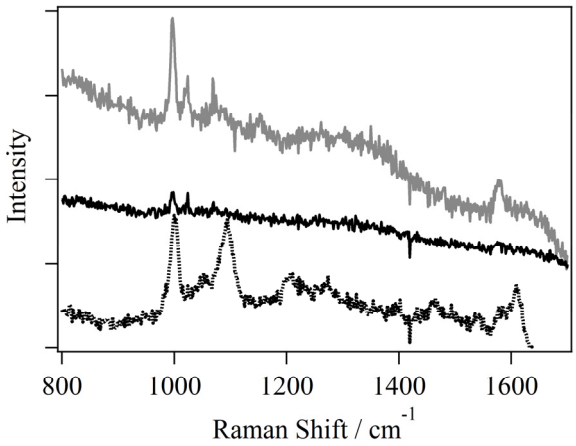

Figure 7. SPR Raman spectra of a sapphire/gold/benzenethiol monolayer/water interface (60 seconds solid black, 180 sec grey) or a sapphire/gold/4-mercaptopyridine monolayer/air interface (60 seconds dotted black). The spectra were acquired at the SPR angle for the respective interfaces.

Supplemental Information

Near IR Scanning Angle Total Internal Reflection Raman Spectroscopy at Smooth Gold Films

*Kristopher J. McKee, Matthew W. Meyer, and Emily A. Smith**

Ames Laboratory, U.S. Department of Energy, and Department of Chemistry, Iowa State University, Ames, Iowa 50011-3111

Figure S1. Schematic of the scanning angle total internal reflection Raman microscope. The excitation beam for collecting bulk Raman spectra travels path “a”, for TIR and SPR Raman spectra the excitation beam travels path “b”. Optics in the dashed boxed are oriented perpendicular to the optical table, and have been offset for clarity.

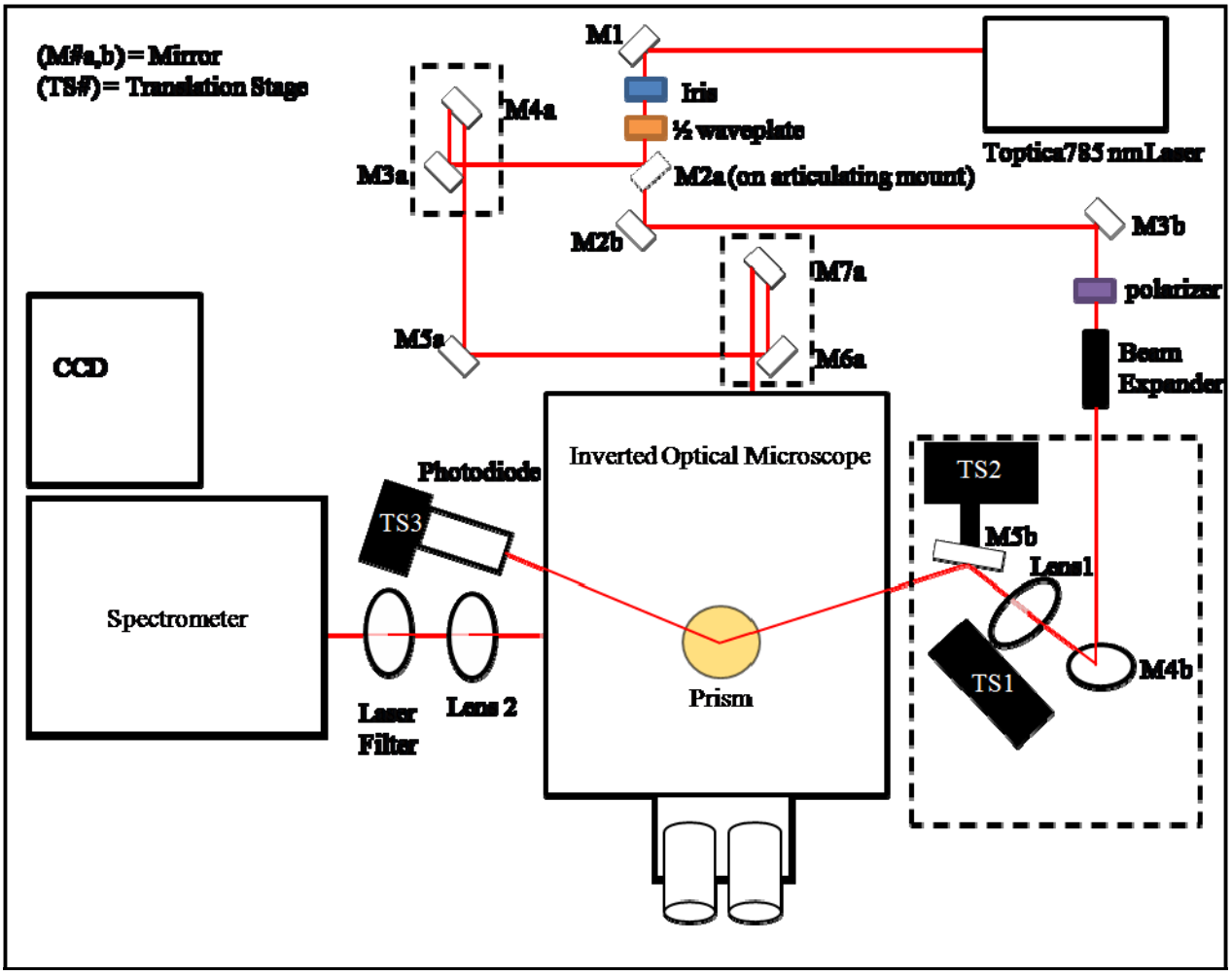

Figure S2. Contact mode AFM image (5x5 µm) of the smooth gold film. The z-scale is 0 to 25 nm and the RMS roughness was measured as 0.639 nm.

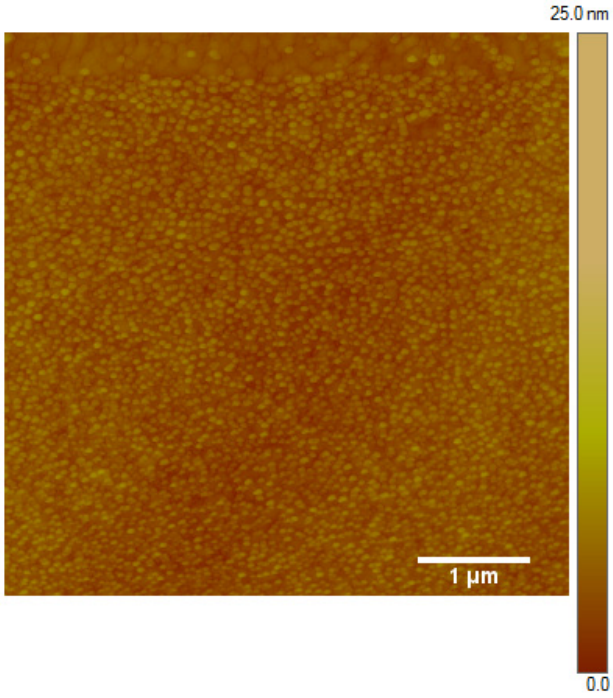

Figure S3. SPR Raman spectra of a washed benzenethiol monolayer (black, benzenthiol monolayer/water interface) and neat benzenethiol (grey) at the SPR angle for each interface, 51.25 and 69.85 degrees, respectively.

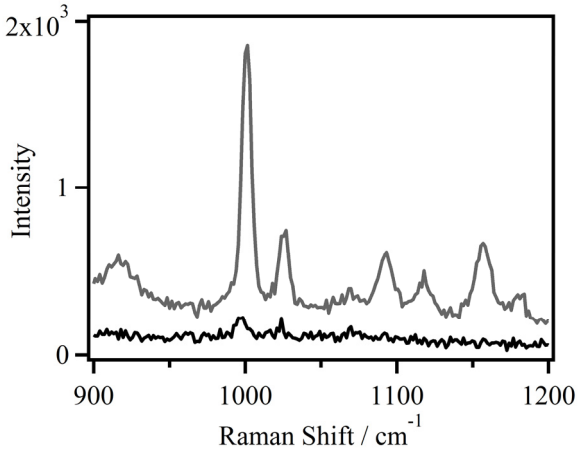

Table S1. Raman peak assignments using Wilson notation.

Pyridine		4-Mercaptopyridine (Gold)		Benzenethiol (Gold)		Nitrobenzene	
Assignment	Raman Shift (cm^{-1})	Assignment	Raman Shift (cm^{-1})	Assignment	Raman Shift (cm^{-1})	Assignment	Raman Shift (cm^{-1})
						6b	611
6a	617					6a	681
						ONO s bend	852
12	1035			12	1002	12	1003
						10b	1021
1	1003	1	998	1	1091	1	1106
18a	1070	18a	1049	18a	1025		
		18b	1093				
				15	1159		
						9b	1162
9a	1218					9a	1172
						NO_2 s stretch	1346
8b	1577	8b	1580			8b	1525
8a	1595	8a	1607	8a	1584	8a	1589

CHAPTER 4: PLASMON WAVEGUIDE RESONANCE RAMAN SPECTROSCOPY

A paper submitted to Analytical Chemistry.

Kristopher J. McKee, Matthew W. Meyer and Emily A. Smith

Ames Laboratory, U. S. Department of Energy, Ames, Iowa 50011-3111, and Department of Chemistry, Iowa State University, Ames, Iowa 50011-3111

Abstract

Raman spectra were collected from a 1.25 M aqueous pyridine solution or a 70-nm polystyrene film at a plasmon waveguide interface under total internal reflection (TIR). The plasmon waveguide interface consisted of a sapphire prism/50-nm Au/550-nm SiO_2. The Raman peak area as a function of incident angle was measured using 785 nm excitation, and was compared to the Raman peak area obtained at a sapphire or sapphire/50-nm Au interface. The Raman scatter from pyridine was enhanced 1.3-fold at a plasmon waveguide compared to spectra collected at a sapphire/Au interface when the signal was adjusted for the number of molecules probed. In contrast to measurements at a bare Au film where only p-polarized incident light generates an enhanced interfacial electric field, plasmon waveguide interfaces enable excitation with orthogonal polarizations using s- or p-polarized incident light. The Raman scatter from a 70-nm polystyrene film was enhanced 3.8- or 4.1-fold using the

plasmon waveguide compared to measurements at the sapphire interface with s- or p-polarized incident light, respectively. The reflected light from the interface was used to quickly identify the incident angle where the maximum Raman scatter was produced, and the Raman signal generated at the plasmon waveguide interface was modeled by the interfacial mean square electric field. In comparison to the techniques on which this work was based (i.e. plasmon waveguide resonance (PWR) spectroscopy, TIR Raman spectroscopy at the prism interface, and surface plasmon resonance (SPR) Raman spectroscopy at the prism/Au interface), chemical specificity was added to PWR spectroscopy, a signal enhancement mechanism was introduced for TIR Raman spectroscopy, and polarization control of the interfacial electric field was added to SPR Raman spectroscopy.

Introduction

Total internal reflection (TIR) Raman spectroscopy measures chemically specific information from an analyte located within a hundred nanometers to a few microns from an interface.[1-10] Under TIR, the illuminating laser light is directed onto a prism/analyte interface at an incident angle higher than the critical angle (Figure 1a). Under these conditions, the Raman signal is confined to the interface as a result of the generated evanescent wave's limited penetration into the sample. Recently, the technique has seen increased use as modern technology has improved signal-to-noise ratios in TIR Raman spectra. The most current studies have focused on the behavior of adsorbates at various substrates and thickness measurements in polymer films.[11-15]

With visible excitation, TIR Raman scatter can be measured from a monolayer of analyte in less than a minute.[11] Despite the benefit for many analytes of reduced spectral background using near IR excitation, acquiring TIR Raman signal from a monolayer has required several minute acquisition times, largely due to the frequency dependence of Raman scatter.[16-17] The use of a thin Au film at the sample interface (Figure 1b) has been shown to enhance the Raman scatter, increase measurement reproducibility, and reduce background in TIR Raman spectroscopy.[18-19] Inclusion of the Au film at the interface increases the interfacial mean-square electric field (MSEF) and the generated Raman scatter at incident angles where surface plasmons are excited in the metal film. A 50-nm Au film, aqueous analyte and 785 nm excitation produces a 25-fold enhancement over an interface without the Au film in the MSEF at the sample interface relative to the incident field. While Raman signal enhancement is expected at the Au interface, only p-polarized incident light excites the surface plasmons in the Au film. This results in a MSEF enhancement primarily in the *z*-direction, and to a minor extent in the *x*-direction (Figure 1). No Raman signal is generated at the Au interface with s-polarized excitation light, and some information regarding the orientation and structure of the analyte layer may not be measured.

Plasmon waveguides were used to reduce the full width half maximum of the reflectivity curves and increase precision in traditional SPR spectroscopy. The technique was coined plasmon waveguide resonance (PWR) spectroscopy.[20] The most prolific use of PWR spectroscopy has been in the biological arena to study cell membrane phenomena.[20-24] In the simplest case, a plasmon waveguide consists of a thin surface plasmon supporting metal film coated with a dielectric layer with a thickness of approximately $\lambda/2\eta$ or greater, where λ is

the excitation wavelength and η is the dielectric's refractive index (Figure 1c).[25] Plasmon waveguides operate by coupling surface plasmon modes in the metal to guided modes within the waveguide. The incident electric field is amplified at the dielectric interface and an evanescent wave is generated in the adjacent medium. The plasmon waveguide substrates enable both p- and s-polarized incident light to generate guided modes in the waveguide, and produce enhanced interfacial electric fields polarized in the *x*-, *y*- and *z*-directions.

In theory, plasmon waveguide substrates enable the characterization of TIR Raman scatter using both parallel and perpendicularly polarized incident light,[26] and increase the amount of Raman scatter generated at the interface. The purpose of this study is to quantify and model the generated Raman scatter at the plasmon waveguide interface and to compare this to the Raman scatter generated at the prism or prism/Au interface. Raman scatter from an aqueous 1.25 M pyridine solution and a 70-nm polystyrene film have been collected. Models to account for the amount of Raman signal generated at the plasmon waveguide interface have been developed.

Materials and Methods

Sample Preparation. Au films were prepared on 25 mm sapphire discs (Meller Optics, Providence, RI) by deposition of 2 nm Ti followed by 49 ± 1 nm of Au (deposition performed by GWC Technologies Inc., Madison, WI). For the waveguide films, 548 ± 2 nm of SiO_2 was deposited on the previously prepared Au films (performed by University of Minnesota Nanofabrication Center, Minneapolis, MN). Film thicknesses were confirmed

using a F20 series film measurement system (Filmetrics, San Diego, CA) operated in transmission mode. A 2% polystyrene (Sigma-Aldrich, St. Louis, MO) solution was prepared in toluene (Fisher Scientific, Waltham, MA) and polystyrene films were then prepared by spin coating 200 μL of the polystyrene solution on bare sapphire disk or a silica plasmon waveguide substrate at 3000 rpm for 1 min using a KW-4A spin coater (Chemat Technology, Inc. Northridge, CA).[27] Prior to coating, the substrates were cleaned in ethanol and dried with a stream of N_2 gas. A 1.25 M pyridine solution (Fisher Scientific, Waltham MA) was prepared in DI water from an Easy Pure II purification system.

Raman Measurements. A previously described scanning angle TIR Raman microscope with 0.05˚ incident angle resolution was used to collect Raman and reflectivity spectra with 200 mW of 785 nm light incident at the sample.[18] The Raman scatter was collected using a 10X 0.30 NA microscope objective and a sapphire prism was used for all measurements. The polarization of the incident light was controlled by rotation of a half-wave plate in the optical path to deliver s- or p-polarized laser light at the sample interface. Measurements of the polarization at the sample indicated that less than 1% of the opposite polarization was present. Raman spectra and reflectivity measurements were acquired simultaneously in 1 minute acquisitions and replicate measurements were obtained from consecutive scans through the incident angle range.

Data Analysis. Peak areas and intensities for the measured Raman modes were calculated by fitting them to Gaussian curves with the "Multipeak fitting 2" algorithm in IGOR Pro 6. The reflected light intensity and MSEF at the interface were modeled with

Fresnel calculations using macros developed in IGOR Pro 6 that allow the incident angle spread to be varied.[28]

The depth over which Raman scatter is collected, D_{RS}, was calculated at the various interfaces using equations 1.1, 1.2 or 3-D finite-difference-time-domain (FDTD) based simulations (EM Explorer, San Francisco, CA). D_{RS} was calculated at the sapphire/analyte interface using the equation:

$$D_{RS} = \frac{\lambda}{4\pi}\left(\frac{\sin^2\theta_i}{\left(\eta_p/\eta_s\right)^2} - 1\right)^{-\frac{1}{2}} \tag{0.1}$$

where η_p and η_s are the refractive indices of the prism and sample at excitation wavelength λ incident on the interface at angle θ_i. At the sapphire/Au/analyte interface, D_{RS} was calculated as:

$$D_{RS} = \frac{\lambda}{4\pi}\left(\frac{\varepsilon'_m + \varepsilon_s}{\varepsilon_s^{\,2}}\right)^{\frac{1}{2}} \tag{0.2}$$

where ε'_m is the real portion of the metal's dielectric constant and ε_s is the dielectric constant of the sample at excitation wavelength λ.The D_{RS} value at the sapphire/Au/SiO_2/analyte interface was calculated from FDTD simulations by plotting the spatial distribution of the MSEF through the film stack. D_{RS} is reported as the point where the MSEF decreases to a value of $1/(2e)$ times the initial MSEF in the analyte layer. The factor of 2 in the denominator accounts for the Raman scatter's proportionality to the square of the electric field.

Results and Discussion

TIR, SPR and PWR Raman scatter of a homogenous solution. The goal of this work is to experimentally test and model the enhanced Raman signals at a plasmon waveguide interface where MSEF enhancements are predicted compared to interfaces without the plasmon waveguide. Figure 1 illustrates the three interfaces studied in this work: (a) represents total internal reflection (TIR) Raman spectroscopy at the prism interface, (b) represents surface plasmon resonance (SPR) Raman spectroscopy at a Au interface, and (c) represents plasmon waveguide resonance (PWR) Raman spectroscopy at a Au/SiO_2 interface. Calculated reflectivity and MSEF curves for the TIR, SPR, and PWR configurations are shown in Figure 2 for a 1.0 index of refraction 'analyte' layer. Reflectivity spectra predict where the maximum Raman scatter for a given interface should be generated. In the TIR case, the critical angle is 34.59˚, corresponding to the largest distance from the interface over which Raman scatter is generated (D_{RS}) and the largest interfacial MSEF. At an SPR interface, the highest interfacial MSEF is generated at the incident angle where the reflected light is maximally attenuated (i.e. the SPR angle, 35.53˚) and corresponds to the excitation of surface plasmons in the metal. D_{RS} is constant at all angles greater than the critical angle in the case of SPR Raman spectroscopy.[29] The reflectivity from a plasmon waveguide shows two minima for p-polarized incident light (42.61˚ and 59.86˚) and a single minimum for s-polarized incident light (49.58˚). The 42.61˚ and 49.58˚ minima correspond to the generation of waveguide modes that amplify the interfacial MSEF and are predicted to be the angles where the highest amount of Raman scatter is generated. Similar to SPR Raman Spectroscopy, D_{RS} is constant in PWR Raman spectroscopy.

Raman spectra from a 1.25 M aqueous pyridine solution are shown in Figure 3 at sapphire (a), Au (b), and Au/SiO_2 plasmon waveguide (c) interfaces. The incident angle where the spectra are collected represents the highest signal generated at each interface. The index of refraction for the pyridine solution is 1.344, and the solution thickness is semi-infinite on the scale of the penetration depth of the evanescent wave for all three interfaces. In order to directly compare the Raman signal from each interface the number of molecules being probed must be accounted for. This is accomplished by considering the depth over which Raman scatter is collected from the interface, D_{RS}. D_{RS} at the critical, SPR and PWR angle are 760 nm, 156 nm and 279 nm, respectively. After adjusting for the amount of analyte probed (Table 1), the PWR Raman spectrum at the SiO_2 plasmon waveguide shows the highest Raman scatter by 1.3 times the SPR Raman signal and 7.0 times the TIR Raman signal for the 1003 cm^{-1} peak and p-polarized incident light. The experimentally measured enhancement for PWR Raman spectroscopy compared to SPR Raman spectroscopy is the same as predicted by the MSEF calculation (1.3 times); although the expected enhancements for both the PWR and SPR Raman interfaces relative to the TIR Raman interface is less than predicted. The plasmon waveguide is optimized for thin film analytes with air below, which may explain why the expected enhancement is lower than calculated. The instrument's angle resolution may also affect the measured Raman signal, as discussed below. Monolayer detection has previously been reported for non-resonant analytes with 785 nm excitation using SPR Raman spectroscopy with similar enhancement factors (4.6 times) as measured for the plasmon waveguide interface (7.0 times) relative to the bare sapphire interface.[18] For s-polarized incident light there is a 1.6 times enhancement in the Raman signal at the plasmon waveguide interface relative to the sapphire interface.

Spectral background from the TIR prism is the main source of background in near IR excitation TIR Raman spectroscopy. Previously, a reduction in the prism background was reported using a 50-nm Au film between the sapphire and analyte layer due to the limited transparency of the Au film.[30] A reduction in the prism background is also expected at the plasmon waveguide interface. On the other hand, the 500-nm SiO_2 film may contribute to the spectral background since the electric field intensity is high in the waveguide supporting medium (i.e., SiO_2). Comparing the sapphire peak intensity in Figure 3, there is a 11-fold or 58-fold reduction in the 750 cm^{-1} sapphire peak in the PWR spectrum compared to the TIR Raman spectrum using p- or s-polarized incident light, respectively. For s-polarized incident light there is a 1.5-fold reduction in the 647 cm^{-1} sapphire peak at the plasmon waveguide interface. The 647 cm^{-1} sapphire peak is completely eliminated in the PWR Raman spectrum with p-polarized incident light, and a 655 cm^{-1} analyte peak is revealed that is not detectable in the TIR Raman spectrum. A silica background is broad across the spectral region shown in Figure 3.[18] Overall, the spectral background is lowest at the PWR spectrum, and no sign of increased silica background is measured.

Comparing the PWR Raman spectra obtained with p- and s-polarized incident light reveals that certain modes produced more scatter with p-polarized excitation. The peaks that have a higher relative intensity with p-polarized incident light are at 618, 1072, 1154, 1221, 1577, and 1595 cm^{-1}. These relative peaks intensities are also higher in the TIR Raman spectrum using p-polarized incident light. The depolarization ratios and peak assignments for the pyridine modes that are enhanced with p-polarized incident light indicate that these modes are asymmetric vibrations (Table 2). For this case of a homogenous pyridine solution,

the differences in the Raman spectra using orthogonally polarized incident light match the known depolarization ratios for these peaks. This is expected because the majority of the PWR or TIR Raman signal is from solution species that are not expected to exhibit any particular orientation. Adsorbate, which may be oriented relative to the interface, contributes no more than ~2% to the signal in this case.[18] The additional spectral information gained using a plasmon waveguide to enhance the Raman signal provides a means to elucidate molecular orientation of adsorbates and thin films, which may not be possible using SPR Raman spectroscopy. Comparing the similar enhancements of the pyridine Raman scatter at the Au and plasmon waveguide interfaces, the main benefits of PWR Raman spectroscopy are: the additional background suppression, additional spectral information available using p- and s-polarized incident light and the possibility of studying a different surface chemistry (SiO_2 vs. Au).

PWR Raman scattering from a thin polystyrene film. Raman spectra from a 70-nm polystyrene film at a sapphire and Au/SiO_2 plasmon waveguide interface are shown in Figure 4. The spectra were collected at the incident angle where the highest signal is obtained at each interface, which was approximately the critical angle (sapphire, 55.48˚) and the PWR angles (SiO_2 plasmon waveguide, 46.81˚ p-polarization and 51.87˚ s-polarization). Similar to what was measured for the pyridine solution, one major difference between the TIR and PWR Raman spectra is the reduction in sapphire background peaks at the plasmon waveguide interface. The prism background obfuscates one of the four polystyrene peaks that are measured at the plasmon waveguide interface (622, 1001, 1034 and 1603 cm^{-1}). In contrast to the Raman spectra of the pyridine solution, all polystyrene peaks at the plasmon

waveguide interface have similar relative intensities within the signal-to-noise ratio using s- and p-polarized incident light. This is consistent with all the assigned peaks having a large depolarization ratio (Table 2).

The reflected light intensity and Raman peak areas as a function of the incident angle at the plasmon waveguide interface are shown in Figure 5 for the 70-nm polystyrene film. The location of the PWR angles are correctly identified in the reflectivity spectra for both p- and s-polarized incident light, although the amount the reflected light intensity is attenuated is experimentally lower than what it should be based on the calculations. This is due to the very narrow PWR peaks compared to the SPR peaks measured at a Au interface. The full width half maximum of the PWR peak is approximately 0.2 and 0.05 degrees using p-and s-polarized incident light, respectively. The instrument's angle resolution is 0.05 degrees. Collecting data at the exact PWR angle is difficult and this explains the discrepancy between the experimental and calculated reflected intensity. The incident angle where the maximum Raman scatter is collected matches the angle of maximum attenuation of the reflected light intensity within the experimental uncertainty. This indicates the reflectivity curve can be used to locate the optimal incident angle for measuring the Raman spectra.

Since the thickness of the 70-nm polystyrene layer is less than the penetration depth of the evanescent wave at all incident angles for both the TIR and PWR interfaces, the same amount of Raman scatterers are being probed at both interfaces. A direct comparison of the Raman peak areas is possible without further consideration of D_{RS}. The Raman peak area for the 1001 cm^{-1} stretching mode is 3.8 and 4.1 times larger in the PWR spectra than in the TIR spectra for s- and p-polarized incident light, respectively. Differences in the Raman peak area

for the polystyrene film at the sapphire or plasmon waveguide interface are due to differences the MSEF generated at each interface. The predicted enhancement of the Raman signal at the plasmon waveguide interface is roughly 11-fold larger than the sapphire interface based on the MSEF calculations. The lower than expected enhancement is a result of the instrument's incident angle resolution compared to the width of the plasmon waveguide mode peaks. Increasing the angle resolution of the instrument and reducing the spread in the incident angle (which is a result of the focusing that takes place within the prism) are predicted to further increase the amount of Raman scatter collected at the plasmon waveguide interface, particularly for the spectrum obtained with s-polarized light.

Conclusions

Previous applications of PWR spectroscopy have not provided chemically specific information, and SPR Raman spectroscopy does not allow measurements of anisotropy or chemical orientation. However, by combining PWR spectroscopy with TIR Raman spectroscopy several benefits are realized. Since the enhancement of Raman signal for analytes at the SiO_2 plasmon waveguides are roughly on par with those measured at smooth Au films, the key benefits of using the plasmon waveguide are the ability to generate both parallel and perpendicular electric fields in the sensing layer, reduced prism backgrounds and the possibility of studying phenomena at the silica interface. The waveguides are not limited to SiO_2, and the benefits and measurement of other dielectric materials is currently being explored.

Acknowledgements

This research is supported by the U.S. Department of Energy, Office of Basic Energy Sciences, Division of Chemical Sciences, Geosciences, and Biosciences through the Ames Laboratory. The Ames Laboratory is operated for the U.S. Department of Energy by Iowa State University under Contract No. DE-AC02-07CH11358. The authors thank the University of Minnesota Nanofabrication Center for assistance in fabricating plasmon waveguides and the Iowa State University Microelectronics Research Center for use of their Filmetrics instrument.

References

(1) Ikeshoji, T.; Ono, Y.; Mizuno, T. *Applied Optics* **1973**, *12*, 2236.

(2) Hoelzer, W.; Schroeter, O.; Richter, A. *Journal of Molecular Structure* **1990**, *217*, 253.

(3) Iwamoto, R.; Miya, M.; Ohta, K.; Mima, S. *Journal of the American Chemical Society* **1980**, *102*, 1212.

(4) Iwamoto, R.; Miya, M.; Ohta, K.; Mima, S. *Journal of Chemical Physics* **1981**, *74*, 4780.

(5) Iwamoto, R.; Ohta, K.; Miya, M.; Mima, S. *Applied Spectroscopy* **1981**, *35*, 584.

(6) Nakanaga, T.; Takenaka, T. *Journal of Physical Chemistry* **1977**, *81*, 645.

(7) Sohn, A. F.; Tisinger, L. G.; Sommer, A. J. *Microscopy and Microanalysis* **2004**, *10(Suppl2)*, 1316.

(8) Takenaka, T.; Nakanaga, T. *Journal of Physical Chemistry* **1976**, *80*, 475.

(9) Tisinger, L. G.; Sommer, A. J. *MIcroscopy and Microanalysis* **2004**, *10*, 1318.

(10) Yoshikawa, M.; Gotoh, T.; Mori, Y.; Iwamoto, M.; Ishida, H. *Applied Physics Letters* **1994**, *64*, 2096.

(11) Woods, D. A.; Bain, C. D. *Analyst (Cambridge, United Kingdom)* **2012**, *137*, 35.

(12) Tyrode, E.; Rutland, M. W.; Bain, C. D. *Journal of the American Chemical Society* **2008**, *130*, 17434.

(13) Woods, D. A.; Petkov, J.; Bain, C. D. *Journal of Physical Chemistry B* **2011**, *115*, 7341.

(14) Woods, D. A.; Petkov, J.; Bain, C. D. *Journal of Physical Chemistry B* **2011**, *115*, 7353.

(15) Kivioja, A. O.; Jaaskelainen, A. S.; Ahtee, V.; Vuorinen, T. *Vibrational Spectroscopy* **2012**, *doi: 10.1016/j.vibspec.2012.02.014*.

(16) McKee, K. J.; Smith, E. A. *Review of Scientific Instruments* **2010**, *81*, 043106/1.

(17) Ishizaki, F.; Kim, M. *Japanese Journal of Applied Physics* **2008**, *47*, 1621.

(18) McKee, K. J.; Meyer, M. W.; Smith, E. A. *Anal. Chem. (Washington, DC, U. S.)* **2012**, *84*, 4300.

(19) Meyer, S. A.; Le Ru, E. C.; Etchegoin, P. G. *Analytical Chemistry (Washington, DC, United States)* **2011**, *83*, 2337.

(20) Salamon, Z.; Macleod, H. M.; Tollin, G. *Biophysical Journal* **1997**, *73*, 2791.

(21) Hruby, V. J.; Alves, I.; Cowell, S.; Salamon, Z.; Tollin, G. *Life Sciences* **2010**, *86*, 569.

(22) Salamon, Z.; Brown, M. F.; Tollin, G. *Trends in Biochemical Sciences* **1999**, *24*, 213.

(23) Salamon, Z.; Tollin, G. *Spectroscopy* **2001**, *15*, 161.

(24) Zhang, H.; Orosz, K. S.; Takahashi, H.; Saavedra, S. S. *Applied Spectroscopy* **2009**, *63*, 1062.

(25) Abbas, A.; Linman, M. J.; Cheng, Q. *Sensors and Actuators B* **2011**, *156*, 169.

(26) Abbas, A.; Linman, M. J.; Cheng, Q. *Biosensors and Bioelectronics* **2011**, *26*, 1815.

(27) Hall, D. B.; Underhill, P.; Torkelson, J. M. *Polymer Engineering and Science* **1998**, *38*, 2039.

(28) *Code for Fresnel calculations was generously made available by Prof. Robert Corn at* http://corninfo.ps.uci.edu/calculations.html.

(29) Raether, H. *Surface Plasmons on Smooth and Rough Surfaces and on Gratings*; Springer-Verlag: Berlin, 1988; Vol. 111.

(30) Boltovets, P. M.; Kravchenko, S. A.; Snopok, B. A. *Plasmonics* **2010**, *5*, 395.

(31) Wu, D.-Y.; Ren, B.; Jiang, Y.-X.; Xu, X.; Tian, Z.-Q. *Journal of Physical Chemistry A* **2002**, *106*, 9042.

(32) Kellar, E. J. C.; Galiotis, C.; Andrews, E. H. *Macromolecules* **1996**, *29*, 3515.

(33) Loader, E. J. *Journal of Catalysis* **1971**, *22*, 41.

(34) Palm, A. *J. Phys. Chem.* **1951**, *55*, 1320.

(35) Ay, F.; Kocabas, A.; Kocabas, C.; Aydinli, A.; Agan, S. *J. Appl. Phys.* **2004**, *96*, 7147.

(36) Malitson, I. H.; Murphy Jr, F. V.; Rodney, W. S. *J. Opt. Soc. Am.* **1958**, *48*, 72.

Table 1. TIR, SPR and PWR distance from the interface over which Raman signal is collected (D_{RS}), experimentally measured signal and enhancements of the Raman signal relative to the TIR interface.

Interface	D_{RS} (nm) Angle (degrees)	Measured 1003 cm^{-1} Peak Area (p- or s-polarization)	Expected Enhancement	Measured Enhancement
TIR Sapphire/pyridine	760 (50.8)	6200 ± 300 (p) 13900 ± 200 (s)		
SPR 50-nm Au/pyridine	156 (> 52.7)	6800 ± 200 (p)	11x	5.3x
PWR 50-nm Au/550-nm SiO_2/pyridine	279 (> 49.2)	16000 ± 300 (p) 8400 ± 100 (s)	8.5x 115x	7.0x 1.6x

Table 2. Raman peak assignments for the indicated analyte at the plasmon waveguide interface and depolarization ratios measured in solution.

Pyridine Peak (cm^{-1})	Assignment[31] (Wilson Notation)	Depolarization Ratio[a]
618	ν_{6a}	-
1003	ν_{1}	0.02
1035	ν_{12}	0.01
1072	ν_{18a}	-
1221	ν_{9a}	0.49
1577	ν_{8b}	0.59
1595	ν_{8a}	-
Polystyrene Peak	**Assignment[32-33]**	**Depolarization Ratio[34]**
622	ν_{6b}	1.00
1001	ν_{12}	0.61
1034	ν_{18a}	0.88
1602	ν_{8a}	1.11

[a] measured using normal Raman spectroscopy (i.e., non-TIR)

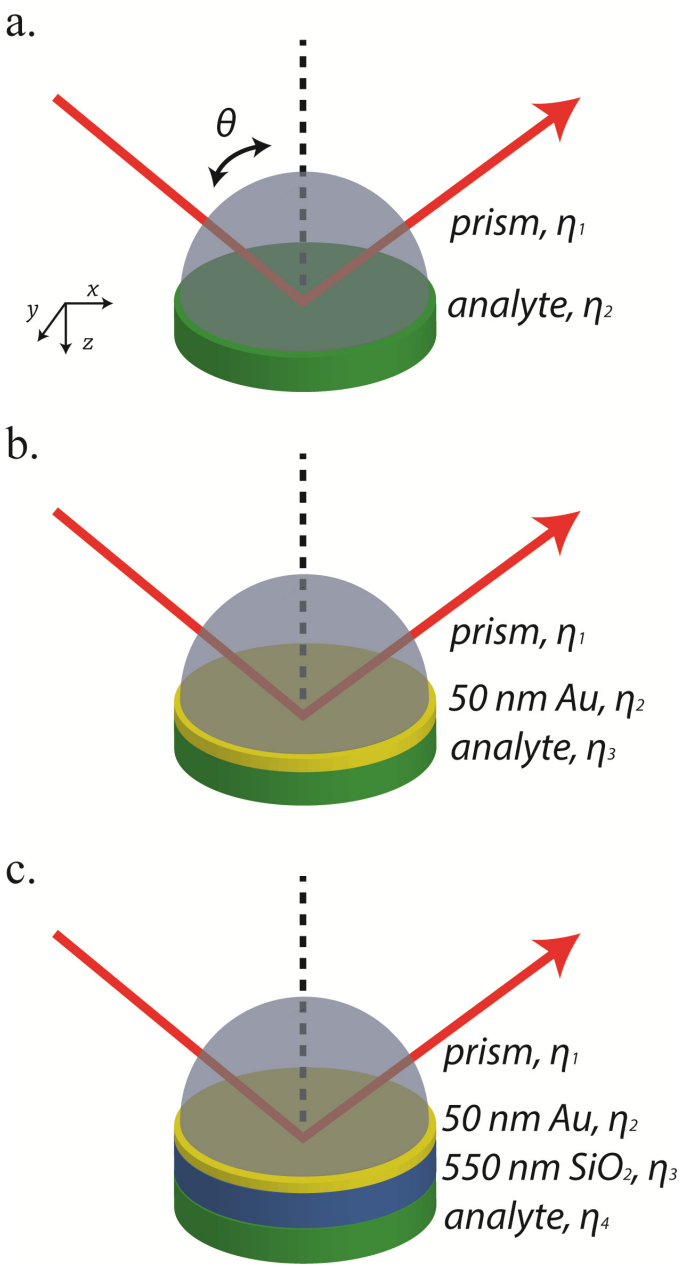

Figure 1. Experimental sample configuration for (a) total internal reflection (TIR) Raman spectroscopy, (b) surface plasmon resonance (SPR) Raman spectroscopy, or (c) plasmon waveguide resonance (PWR) Raman spectroscopy. The axes represents the orientation referred to throughout the text where the *z*-axis is perpendicular to the interface and the *y*-axis extends towards the reader. In all experiments η_1 is a sapphire prism.

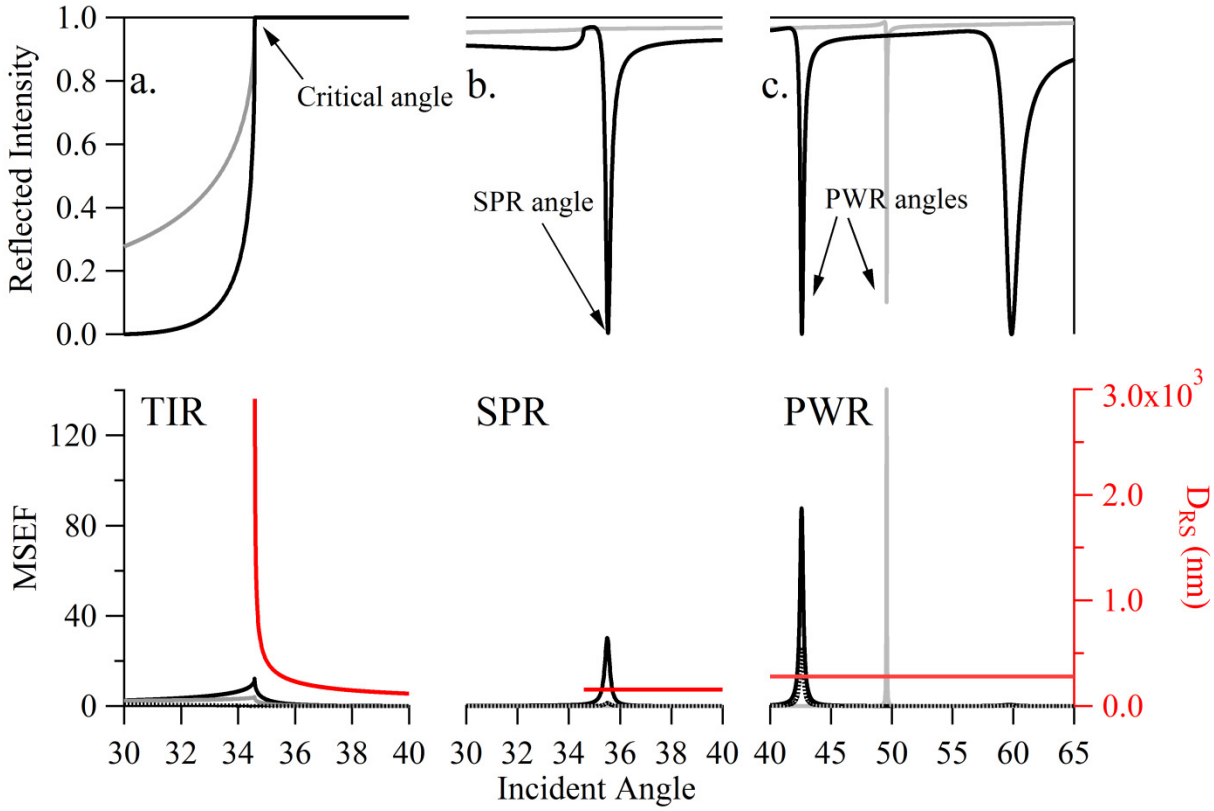

Figure 2. The calculated intensity of light reflected from the interface (top), corresponding mean-squared electric field relative to the incident field (bottom, left axis) and depth over which Raman scatter is collected, D_{RS}, (bottom, right axis) for a: (a) sapphire/air (TIR) interface, (b) 50-nm Au/air (SPR) interface, or (c) 50-nm Au/550-nm SiO_2 plasmon waveguide/air (PWR) interface and p- (black) or s- (grey) polarized 785 nm incident light. P-polarized incident light generates electric fields polarized in the *x* (black dotted) and *z* (black solid) planes and s-polarized light generates an electric field polarized in the *y* plane (gray solid).

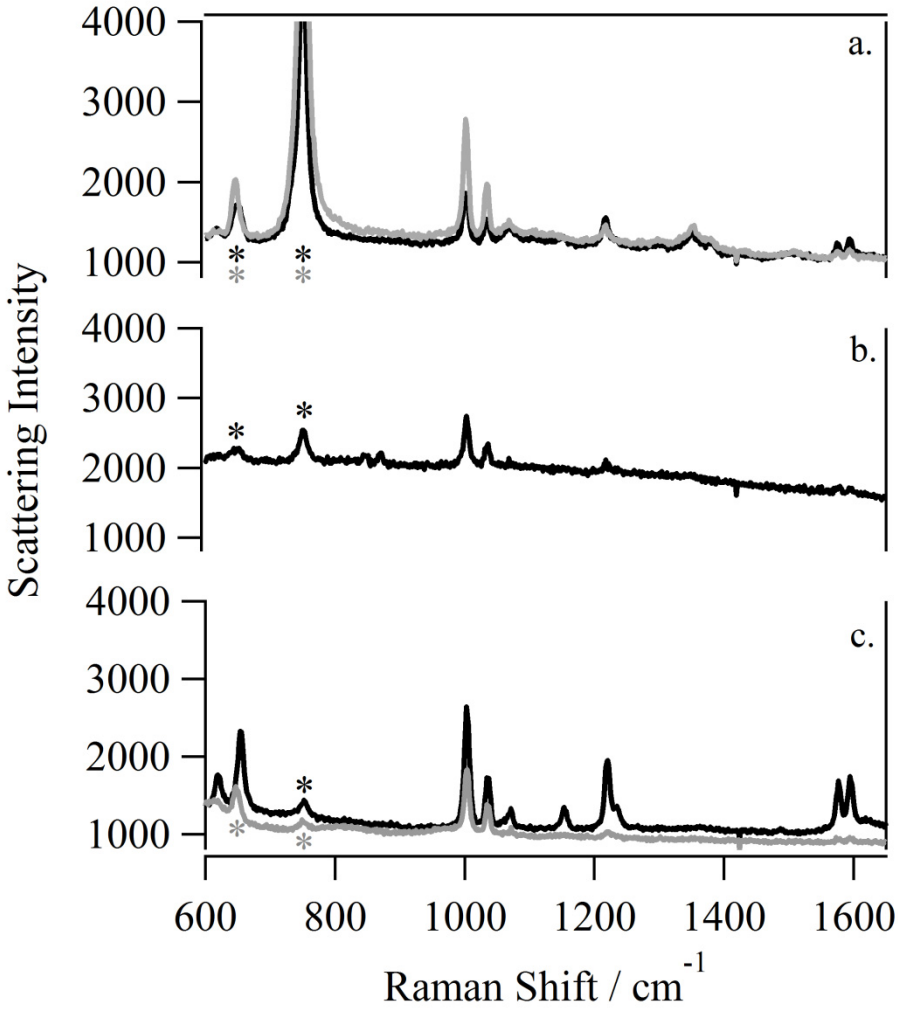

Figure 3. Raman spectra of pyridine at a: (a) sapphire (TIR) interface, (b) 50-nm Au (SPR) interface, or (c) 50-nm Au/550-nm SiO_2 plasmon waveguide (PWR) interface and p- (black) or s- (grey) polarized 785 nm incident light. The spectra were collected near the critical (50.5˚), SPR (52.90˚), or PWR (p-polarization: 49.20˚, s-polarization: 51.08˚) angle, respectively. These are the angles where the largest Raman scatter is collected at each interface. The discrepancy between the experimental and calculated critical, SPR, or PWR angle is within 0.25 degrees. The asterisks (*) represent peaks that originate from the sapphire prism.

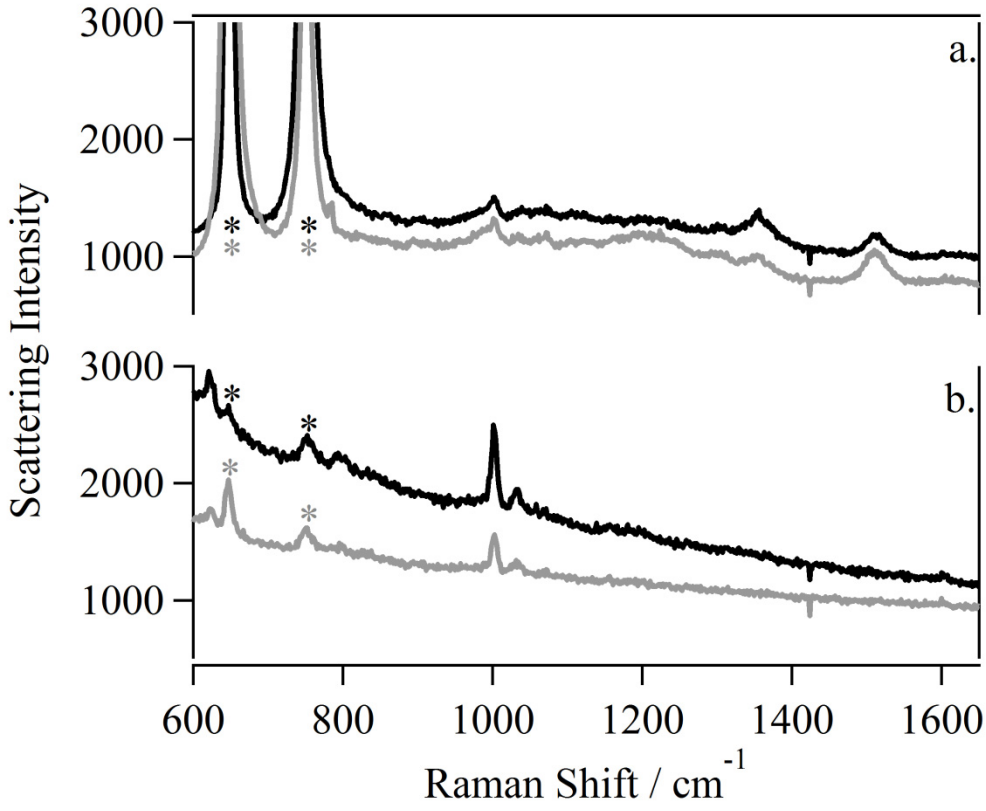

Figure 4. Raman spectra from a 70-nm polystyrene film at a (a) sapphire (TIR) interface, (b) 50-nm Au/550-nm SiO_2 plasmon waveguide (PWR) interface and p- (black) or s- (grey) polarized 785 nm incident light. The spectra were collected at (a) (53.48˚) or (b) (p-polarization: 46.77˚ and s-polarization: 51.87˚), which is close to the critical angle or PWR angles and where the largest Raman scatter is collected at each interface. The asterisks (*) represent peaks that are from the sapphire prism.

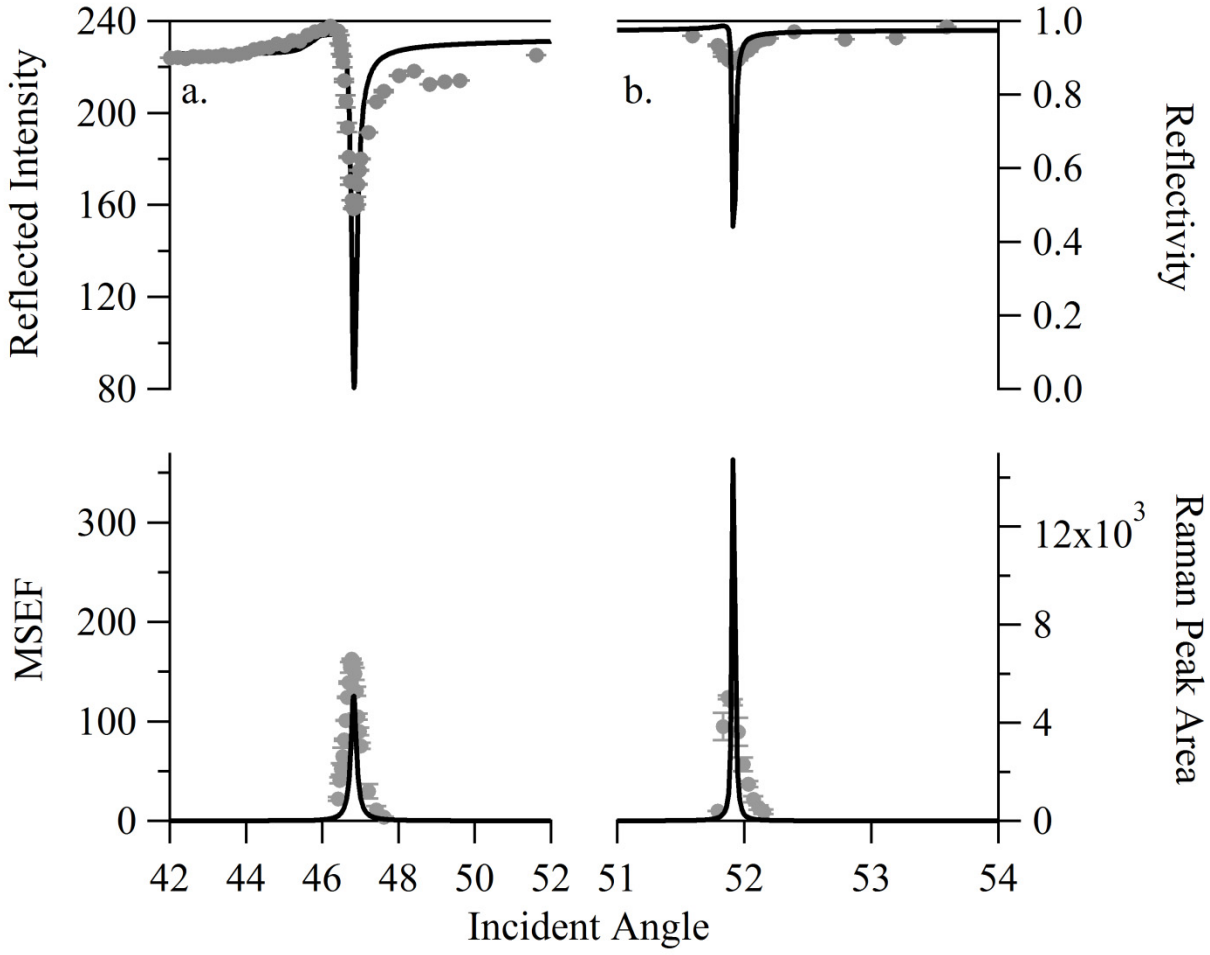

Figure 5. Experimental reflectivity spectra (gray symbols, top) and Raman peak areas (gray symbols, bottom) from a 70-nm polystyrene film coated on a 50-nm Au/550-nm silica plasmon waveguide with (a) p- polarized or (b) s-polarized incident light and 785 nm excitation. Waveguide modes are generated at 51.87˚ with s-polarized incident light and 46.77˚ with p-polarized incident light. The data are fit to Fresnel reflectivity coefficients (black line, top) or calculated interfacial mean square electric fields relative to the incident field (MSEF, black line, bottom). The calculated reflectivity and MSEF curves account for the anisotropy of the sapphire prism and polystyrene film.[35-36]

CHAPTER 5: GENERAL CONCLUSIONS

This dissertation is focused on the development of a scanning angle total internal reflection Raman spectrometer based on an inverted wide field microscope and surface plasmon based signal enhancement strategies for use with near infrared excitation. The instrument that was built delivers an excitation beam to a prism / sample interface over a large incident angle range (≈ 50˚) with 0.05˚ angular resolution enabling control over the depth that Raman scatter is generated in the sample. The large incident angle range allows TIR Raman measurements to be collected for a wide variety of prism material (eg. BK-7, SF11, sapphire, ZnSe) and sample matrix (eg. air, water, organic solvent) combinations. Techniques for modeling the Raman scatter collected at various incident angles were developed where compensation for the spread of incident angles reaching the sample interface was required. Sub-micrometer probe depths and near infrared excitation necessitated relatively long acquisition times leading to the exploration of signal enhancement strategies.

A reproducible Raman scattering enhancement strategy for the TIR illumination geometry is developed by including a smooth, thin 50-nm gold film between the prism and sample. With a p-polarized excitation source at the proper angle, surface plasmons are excited in the gold film and the result is an increased electric field at the gold / sample interface. The Raman scatter from analytes at air, water, and organic interfaces is enhanced and monolayer level detection is demonstrated. The use of a gold film at the interface

provides the additional benefits of decreasing the background from system optics, and increasing the reproducibility of the measurement.

Lastly, plasmon waveguides are developed for use in the TIR Raman configuration. Both p- and s- polarized incident light generate electric fields polarized perpendicularly to one another at the waveguide surface under appropriate excitation conditions providing similar enhancement factors and additional spectroscopic information not obtainable when using a thin gold film without a dielectric layer at the interface. Enhanced Raman scatter was demonstrated for analyte both in solution and cast as a film on the waveguide surface.